学位論文

Measurement of the $^{8}Li(\alpha,n)^{11}B$ Reaction with the Multiple-Sampling and Tracking Proportional Chamber for Astrophysical Interest

多重飛跡測定用ガス検出器を用いた、天体核反応 $^{8}Li(\alpha,n)^{11}B$ の測定

平成１１年６月博士（理学）申請
東京大学大学院理学系研究科
物理学専攻
瀬井浩

Measurement of the ^{8}Li(α,n)^{11}B Reaction with the Multiple-Sampling and Tracking Proportional Chamber for Astrophysical Interest

Doctral Dissertation
by
Yutaka Mizoi

June 25, 1999
Revised on August 31, 1999

Contents

Chapter 1

Introduction

1.1 Nucleosynthesis involving unstable nuclei in the early universe

The standard Big-Bang models (SMs) have succeeded in the primordial nucleosynthesis of light elements. In these models, the predicted abundances of light elements up to $A^1 = 7$, which are presumed to be synthesized in the first three minutes of hot Big-Bang expansion, are in good agreement with the observed ones in the oldest-metal-poor stars, if the baryon density of the universe is $0.03 \leq \Omega_B h_{50}^2 \leq 0.06$ [1, 2]. Here, Ω_B is the ratio of the present baryon density to the critical density, $\Omega_B = \rho_B/\rho_C$, h_{50} is the Hubble constant, H_0, divided by 50 km/Mpc/sec and its range is $0.8 < h_{50} < 2.0$, and ρ_C is the critical density[2] which marginally closes the universe.

On the other hand, the total mass density of the universe, which is estimated by observations of the mass-luminosity ratio in the cluster or super cluster of galaxy scales $1 \sim 20$ Mpc, turns out to be $\Omega_0 = 0.3 \sim 1.2$ [3]. Here, the subscript 0 means the present value. The difference, $\Omega_B << \Omega_0$, suggests the existence of invisible mass, which is the so-called dark matter [1, 2].

Recent observations [4] of rich clusters of galaxies have indicated very large baryon fraction, $\Omega_B/\Omega_0 = (0.2 \sim 0.3)h_{50}^{-3/2}$. In the marginally closed-universe model, $\Omega_0 = 1$, the baryon-density parameter becomes $\Omega_B = (0.2 \sim 0.3)h_{50}^{-3/2}$, which is many times larger than the SMs prediction. In another cosmological model of the flat universe $\Omega_0 + \Lambda_0 = 1$ with, for example, $\Omega_0 = 0.3$ and $\Lambda_0 = 0.7$, where Λ_0 is the cosmological constant, it becomes $\Omega_B = (0.06 \sim 0.09)h_{50}^{-3/2}$, being marginally consistent with the SMs prediction. It is controversial whether we need finite Λ_0 or not, in order to make a model of the real universe. Therefore, it is still important and critical to look for the reason that the observed baryon fraction, $\Omega_B/\Omega_0 = (0.2 \sim 0.3)h_{50}^{-3/2}$, is likely to be larger than the SMs prediction, $0.03 \leq \Omega_B h_{50}^2 \leq 0.06$.

Recently, inhomogeneous Big-Bang models (IMs), which allow larger $\Omega_B \sim 0.2h_5^{-3/2}$ than that of the SMs prediction, have been proposed and intensively studied [5, 6, 7, 8, 9, 10]. Although, it seems that, even in the IMs, the marginally closed universe with only baryons, $\Omega_B = 1$, is ruled out, the predicted Ω_B can explain the large baryon fraction as observed in rich clusters in the universe model for $\Omega_0 = 1$.

The IMs assume that the baryon density in the early universe was inhomogeneous, while the SMs assume a homogeneous baryon density. One candidate for the origin of inhomogeneity is based on the quark-hadron phase transition occurring around 10^{-5} sec after the Big Bang according to expanding and cooling the universe, if its transition is of first order. A locally inhomogeneous baryon plasma is produced by a first-order quark-hadron phase transition. In addition, because the neutrons diffuse out from the baryon plasma more easily than do the protons, which are attracted by the electrons, high-density regions which are proton rich and low-density regions which are neutron rich would be produced. In order to reproduce the observed light-element abundances, a high baryon density of $\Omega_B \sim 0.2 - 1.0$ is required in the IM universe, while ^{7}Li might be over-produced. However, recent astronomical observations of deuterium absorption line in Lyman-α clouds along the line of sight to high red-shift quasars have suggested new interpretation of the observed ^{7}Li abundance. Namely, the observed ^{7}Li abundance level in oldest-metal-poor stars is the result of large depletion[3] from higher primordial value, which is consistent with the IMs prediction, and that both deuterium and lithium abundances are explained in the IMs with $\Omega_B \sim 0.2$ [11].

A big difference is found for elements above A = 12; namely, the abundances predicted by the IMs are much larger than those of the SM prediction by a few orders of magnitude, because neutron-rich nuclides play important roles to synthesize heavier elements in the IM universe. Figure 1.1 shows the reaction network around A = 12. Heavier elements are formed when the temperature of the universe is near $T_9 = 1$ ($T_9 = 10^9$ K).

In particular, the main path in IM nucleosynthesis is

$$^1\mathrm{H}(\mathrm{n},\gamma)^2\mathrm{H}(\mathrm{n},\gamma)^3\mathrm{H}(\mathrm{d},\mathrm{n})^4\mathrm{He}(\mathrm{t},\gamma)^7\mathrm{Li}(\mathrm{n},\gamma)^8\mathrm{Li}(\alpha,\mathrm{n})^{11}\mathrm{B}(\mathrm{n},\gamma)^{12}\mathrm{B}(\beta\nu)^{12}\mathrm{C},$$

where ^{8}Li, whose half life is 840 msec, is the key element, while the three-body reaction $3\alpha \rightarrow {}^{12}$C is the main path in SM nucleosynthesis.

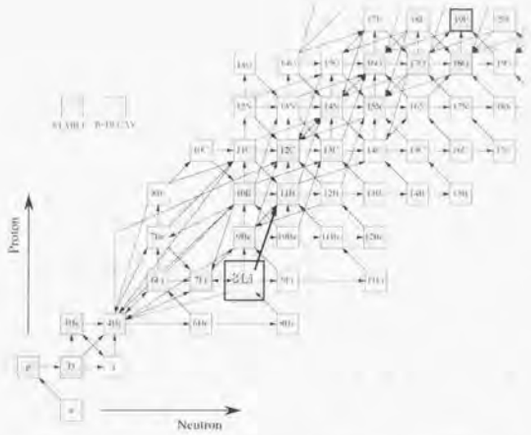

Figure 1.1: Reaction-network diagram. The reaction chains considered in the IMs are shown. The horizontal axis is the number of neutrons and the vertical axis is the number of protons. The white box shows the β-decay nuclei and the gray box shows the stable nuclei.

[1] A is the atomic mass number.

[2] $\rho_C = 3H_0^2/8\pi G$; G is the gravitational constant.

[3] In stellar burning, ^{7}Li is easily destroyed by the ^{7}Li(p,α)^{4}He reaction.

Another weaker (~15%) chain path is also opened,

$$^{1}\mathrm{H}(\mathrm{n},\gamma)^{2}\mathrm{H}(\mathrm{n},\gamma)^{3}\mathrm{H}(\mathrm{d},\mathrm{n})^{4}\mathrm{He}(\mathrm{t},\gamma)^{7}\mathrm{Li}(\alpha,\gamma)^{11}\mathrm{B}(\mathrm{n},\gamma)^{12}\mathrm{B}(\beta\nu)^{12}\mathrm{C}.$$

On the other hand, the ^{8}Li(n,γ)^{9}Li and ^{8}Li(d,n)^{9}Be reactions compete with them and exhaust ^{8}Li, up to 50% [9].

In order to investigate the feasibility of the IMs, the abundances of the elements should be calculated extensively over the entire reaction network. However, those neutron-rich nuclides which take part in IM nucleosynthesis are mostly unstable against β-decay, and therefore their cross-section data which can be used to calculate nucleosynthesis are limited, because it is difficult to perform experiments to measure them.

This thesis involved a measurement of the key reaction for IMs, ^{8}Li(α,n)^{11}B, using a new technique, which is described in the following.

1.2 ^{8}Li(α,n)^{11}B reaction

Some experiments concerning the ^{8}Li(α,n)^{11}B reaction have been performed, in spite of the difficulties due to the short lifetime of ^{8}Li.

One experiment using an inverse reaction, ^{11}B(n,α)^{8}Li, was performed by T. Paradellis et al. [12], which provides an excitation function for the cross section of the ^{8}Li(α,n)^{11}B(ground state) reaction. Other experiments involving a *direct-inclusive measurement* with a Multiple-Sampling Ionization Chamber (MUSIC)-type detector [13] were performed by R. N. Boyd et al. [14] at RIKEN and X. Gu et al. [15] at the Notre-Dame-Michigan-Ohio State radioactive-beam facility, which provide an excitation function of the cross section of the ^{8}Li(α,n)^{11}B(all states) reaction. Figure 1.2 shows the results of their measurements.

The observed cross section of the latter is five-times larger than that of the former at energy regions where their cross sections overlap. Discrepancy between them is attributed to a difference in the final states of ^{11}B; the former includes only the ground-state transition, whereas the latter includes the excited states as well. However, the latter measurements have not directly observed the individual final states of the ^{8}Li(α,n)^{11}B reaction.

On the other hand, S. Kubono et al. [16, 17] and Z. Q. Mao et al. [18, 19] measured the branching ratio from the excited state of ^{12}B to the various states of ^{11}B through the ^{9}Be(α,p)^{12}B*(n)^{11}B reaction. These experiments observed a decay from specific levels of ^{12}B* near to an excitation energy of 10.6 MeV, which is within the Gamov peak of $T_9 = 1$, but the agreement of both experiments is not good. In addition, their experiments may not populate all of the intermediate states relevant to the ^{8}Li(α,n)^{11}B reaction. A summary of their measurement is given in table 1.1. The level scheme relevant to the ^{8}Li(α,n)^{11}B reaction is shown in figure 1.3.

There is no explicit evidence to indicate that the total cross section is five-times larger than the ground-state cross section. Because the total cross section is important for estimating the abundances of the elements, we should know the total cross section without the ambiguity. Therefore, in order to solve the problems, a *direct-exclusive measurement* should be performed to determine the excitation function of the cross section and the branching ratio of the ^{8}Li(α,n)^{11}B reaction. Hence, we performed, for the first time, a *direct-exclusive measurement* with the Multiple-Sampling and Tracking Proportional Chamber (MSTPC) [20], which is designed to measure reactions involving unstable nuclides in the low-energy region.

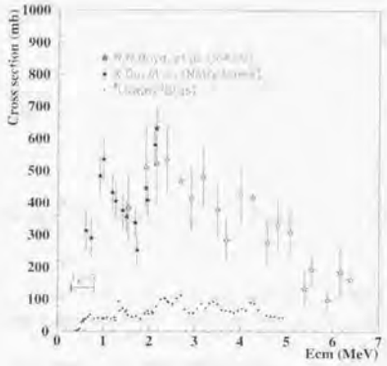

Figure 1.2: Excitation functions of the cross section measured by the inverse reaction and *direct-inclusive measurements*. The horizontal axis is the center-of-mass energy (MeV) and the vertical axis is the cross section (mb). The white stars show the data of the *direct-inclusive measurement* at RIKEN and the black stars show that at Notre Dame. The dots show the data from the measurement by the inverse reaction.

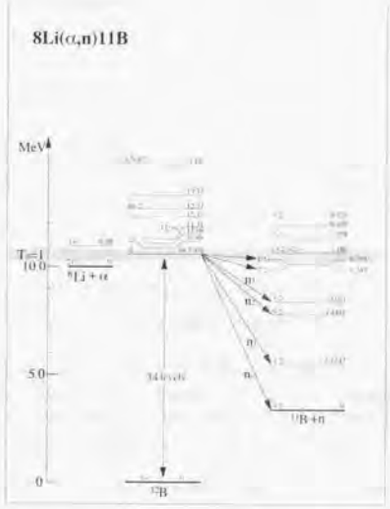

Figure 1.3: Level scheme relevant to the ^{8}Li(α,n)^{11}B reaction. The vertical axis is the reaction energy of the ^{8}Li(α,n)^{11}B and ^{11}B(n,α)^{8}Li reactions, and the excitation energy of ^{12}B in MeV. The ground state of ^{12}B is set to the origin of the energy scale. The gray band indicates the Gamov peak of $T_9 = 1$.

S. Kubono et al. [16, 17]						
^{12}B				Γ_n/Γ		
Ex (MeV)	J^π	n_0	n_1	n_2	n_3	Total
10.572	2^-	0.34	0.04	0.17	0.12	0.67

Z. Q. Mao et al. [18, 19]						
^{12}B				Γ_n/Γ		
Ex (MeV)	J^π	n_0	n_1	n_2	n_3	Total
10.880	3^+	0.12±0.02	0.07±0.01	0.58±0.08	0.14±0.02	0.80±0.05
10.564	2^-	0.15±0.03	0.12±0.02	0.47±0.05	0.16±0.05	0.80±0.05
10.417	$<1^-$	n_0+n_1=0.78±0.24		n_2+n_3=0.58±0.23		1.25±0.25
10.199	2^-	0.19±0.02	0.15±0.02	0.50±0.06	0.13±0.02	0.85±0.05

Table 1.1: Summary of the branching-ratio measurements. The upper table is the result of S. Kubono et al., and the lower table is the result of Z. Q. Mao et al.. The left-hand two columns are the excitation energy, spin and parity of ^{12}B: n_i means the neutron decay to the ith state of ^{11}B. The ^{12}B state of 10.572 MeV in the upper table should correspond to the state of 10.564 MeV in the lower table. The former n_0-branching ratio is not consistent with the latter one.

1.3 New techniques and detectors for experiments with the radioactive isotope beams

The recent developments of ion sources and accelerator techniques have not only improved the intensity of unstable-nuclear beams, the so-called radioactive-isotope (RI) beams, but have also extended the RI species far from the β-stability line.

In parallel with the improvement of beam techniques, experimental techniques have also been developed. The more the RI species are far from the β-stability line, the more are the measurements of nuclear reactions involving the RI beams difficult to perform, due to the limited beam intensity. Therefore, a detector which can measure reactions with sufficient detection efficiency, and a technique which can be used to perform experiments effectively, are required to compensate for the limited beam intensity. While many experiments to measure reactions have been performed at the intermediate energy regions, a few ten MeV/nucleon, for example elastic scattering, Coulomb excitation and so on, reaction measurements at the low-energy region near to the Coulomb barrier have been few, because it is difficult to obtain a low-energy RI beam with sufficient intensity.

We have developed new detectors and experimental techniques to measure fusion reactions near to the Coulomb barrier involving the RI beams [21, 22]. They are a detector system of a multiple stacked target with MWPCs[4] or large-area SSDs[5]. As a powerful detector system which is applicable to a wide range of reaction types, the Multiple-Sampling and Tracking Chamber (MSTPC) was designed and constructed.

The MSTPC has the characteristics of both the Multiple-Sampling Ionization Chamber (MUSIC) [23] and the Time-Projection Chamber (TPC). The MUSIC measures the stopping power (dE/dx) along the particle trajectory passing through the detector gases. The TPC can measure

[4]Multiple-Wire Proportional Chamber.
[5]Si Solid-State Detector

the three-dimensional trajectory of multiple particles. The MSTPC can measure dE/dx along a track for multiple particles by being in-cooperated with the techniques of MUSIC and TPC, thus providing high performance in the event-selection capability. In addition, by utilizing the detector gases as targets, a so-called active target, the MSTPC can detect reactions with a sufficiently thick target without loosing energy information; therefore, the detection efficiency can be sufficiently high. The circuits and data-acquisition system necessary for operating the MSTPC have also been developed. The details concerning the MSTPC are described in Chapter 3.

1.4 Brief summary of the present work

The experiment to measure the ^{8}Li(α,n)^{11}B reaction directly and exclusively with the MSTPC was carried out at the RIKEN Accelerator Research Facility (RARF). At the same time, the ^{9}Be(α,n)^{12}C reaction, which has a similar reaction property and whose data are available [24, 25, 26, 27, 28], was also measured by the present system in order to check the reliability of the present method.

It has been proved that the present measurement system and analysis procedure are effective to measure the I(α,n)J-type reaction and to determine its reaction properties, by comparing the measurement and the known data of the ^{9}Be(α,n)^{12}C reaction. The excitation function of the cross section of the ^{8}Li(α,n)^{11}B reaction and the averaged branching ratio to the various final states of ^{11}B have been determined by the present *direct-exclusive measurement* using the MSTPC with neutron counters. The present result shows that the production cross section of ^{11}B is larger than the cross section derived from the inverse reaction [12] by a factor of 2.6, rather than by a factor of 5, which is claimed at the *direct-inclusive measurements* [14, 15].

The development of the MSTPC is described in Chapter 3 and other applications of the MSTPC are described in Appendix C. The measurement of the ^{8}Li(α,n)^{11}B reaction is described in Chapter 2, and the simulation and analysis procedure are described in Chapter 4 and 5, respectively. The result of the ^{8}Li(α,n)^{11}B-reaction measurement and the discussions about the role of the ^{8}Li(α,n)^{11}B reaction in primordial nucleosynthesis are described in Chapter 6

Chapter 2

Details of the experiment

The experiment was carried out using the RIKEN Projectile-fragment Separator (RIPS) [29] at the RIKEN Accelerator Research Facility (RARF) [30] from September 18th through 25th, 1996. The details of the experimental setup and the procedures are described in this chapter.

2.1 Overview of the experiment

The experiment was designed for a *direct-exclusive measurement* of the ^{8}Li$(\sigma,n)^{11}$B reaction in order to determine the branching ratio to the various excited states as well as to the ground state of ^{11}B. Figure 2.1 shows a schematic view of the experimental setup, which consisted of an apparatus for producing low-energy RI beams and detectors for measuring the reactions. The former consisted of a fragment separator (RIPS) and an energy degrader, and the latter consisted of a time-of-flight (TOF) system for measuring the beam energy, neutron counters and the MSTPC filled with He gas which serves as a target and also works as a detector gas. The details of the individual apparatus are described in the following.

In order to verify the present experimental procedures, the ^{9}Be$(\sigma,n)^{12}$C reaction was also measured by the same system. The ^{9}Be$(\sigma,n)^{12}$C reaction has a similar property as that of the ^{8}Li$(\sigma,n)^{11}$B reaction, as shown in figure 2.14. The excitation functions of the cross section and the individual properties of the ^{9}Be$(\sigma,n)^{12}$C reaction were well measured [24, 25, 26, 27, 28].

Because the iso-butane gas was mixed with He gas for stable operation of the MSTPC, a 5%-isobutane-mixed gas and a 10%-isobutane-mixed gas were used in order to estimate any background effect due to mixed gases in the both measurements of the ^{8}Li$(\sigma,n)^{11}$B and ^{9}Be$(\sigma,n)^{12}$C reactions.

2.2 Low-energy-^{8}Li and ^{9}Be beam production

2.2.1 Primary beam and target

^{8}Li and ^{9}Be were produced through a projectile-fragmentation reaction by irradiating ^{12}C on a 832 mg/cm^2 thick ^{9}Be target. The ^{12}C was ionized by the electron-cyclotron-resonance (ECR) ion source and accelerated up to the energy of 70 MeV/nucleon with an intensity of 60 pnA[1] by a four sector ring cyclotron (K = 540) with the injection AVF cyclotron (K = 70). The species and energy of the primary beam were determined according to the RARF's operation data in order to make the ^{12}C beam optimum.

[1] pnA = particle-nano-Ampere

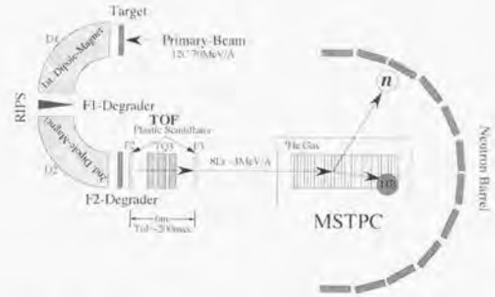

Figure 2.1: Schematic view of the experimental setup. ^{8}Li and ^{9}Be beams are produced by a projectile-fragmentation reaction, selected and collected by the RIPS. The energies of ^{8}Li and ^{9}Be are degraded by the Al-plate and determined by the TOF method. After a TOF measurement, the beams are injected into the MSTPC filled with gases of ^{4}He admixed with 10% or 5% iso-butane at 400 torr pressure. The neutron counters surround the MSTPC from 0 to 90 degrees.

The target thickness was selected in order to maximize the production rate of the ^{8}Li beam by a computer simulation. The yield of the ^{8}Li beam is a function of the target thickness and the accepted momentum. Although a thicker target provides a larger yield, the momentum spread becomes wider and a fraction of beams within the acceptance decreases. Figure 2.2 shows the result of a yield calculation by a computer code, INTENSITY-3 [31], which took into account the production rate of ^{8}Li and the momentum acceptance of the RIPS. The target thickness was determined to be 832 mg/cm^2 according to this result.

For ^{9}Be beam production, the target thickness was not optimized and the same target was used, because the yield of ^{9}Be was much larger than ^{8}Li.

2.2.2 Secondary beam

Fragment separator, RIPS

Not only ^{8}Li and ^{9}Be, but also other nuclear species, are produced through the projectile-fragmentation reaction, and only ^{8}Li or ^{9}Be must be selected by the fragment separator. The RIPS is an apparatus for selecting and collecting specific nuclides, and for providing a secondary beam of specific nuclide. The principle of separation is briefly described in the following.

The separation method is based on a momentum analysis of the magnetic rigidities of the fragments and the their energy losses passing through a material. The collection method is based on the achromatic focus; the separated fragments are to be focused on a small spot regardless of their initial energies.

As one of the best ways to conduct isotopic separation and secondary-beam production [32], the RIPS consists of two dipole magnets for momentum analysis and an energy degrader between two dipole magnets. By the first dipole magnet (D1), the fragments are separated by A/Z, where Z is the atomic number and A is the mass number, because almost all projectile fragments have

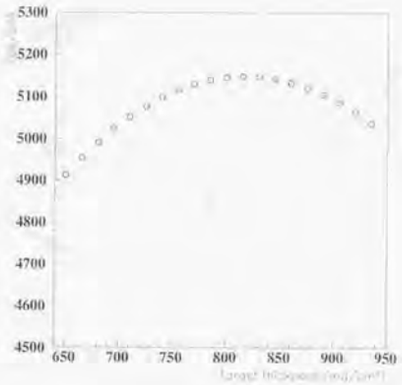

Figure 2.2: Calculated yield of the ^{8}Li beam as a function of the target thickness. The horizontal axis is the ^{9}Be target thickness (mg/cm^2) and the vertical axis is the beam intensity of ^{8}Li (cps/pnA).

the same velocity. The energy losses[2] passing through the energy degrader depend on A and Z of the fragments. Thus, a specific nuclide is separated by the second dipole magnet (D2). As the energy degrader, namely an achromatic degrader, which has a special wedge shape so as not to change the dispersion, is used in the separator.

The RIPS has three focal planes: the first (F1) is between D1 and D2, where the achromatic degrader is located; the second (F2) is after D2 and the third (F3) is downstream of F2, where there is the triplet-quadrupole-magnet (TQ3) system between F2 and F3. The other focusing elements, quadrupole magnets and sextupole magnets are also installed for adjusting higher-order optics.

Particle Identification

Figures 2.3 and 2.4 show a particle identification (PI) plot for selecting ^{8}Li. The former is a picture before inserting the achromatic degrader and the latter is one after inserting the degrader. The vertical axis shows the energy loss, dE (MeV), at F3 measured by the 500 μm-thick and 50×50 mm^2-area pin type SSD[3] which has a 1.5 μm-dead layer. The energy losses through its dead layer were corrected for in all of the present analyses. The horizontal axis shows the TOF (nsec) between F2 and F3, whose flight-path length is 5.299 m. The TOF was measured by a 2 mm-thick, 80×80 mm^2-area-plastic scintillator at F2 and an about 65 μm-thick, 50 mm$^\phi$-plastic scintillator at F3. Figure 2.3 shows that many nuclear species arrived at F3 before the achromatic degrader was inserted. Figure 2.4 shows that only ^{8}Li arrived at F3 after the achromatic degrader was inserted. The species of nuclides were determined by the dE and TOF,

[2] $\Delta E \propto Z^2/A\beta$.
[3] Si Solid-State Detector

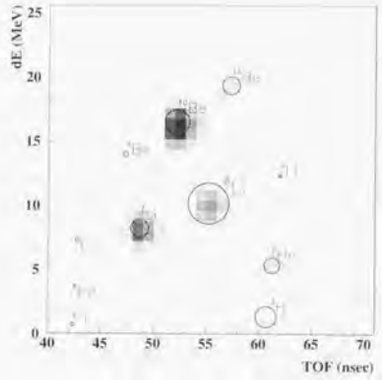

Figure 2.3: PI plot before inserting the achromatic degrader.

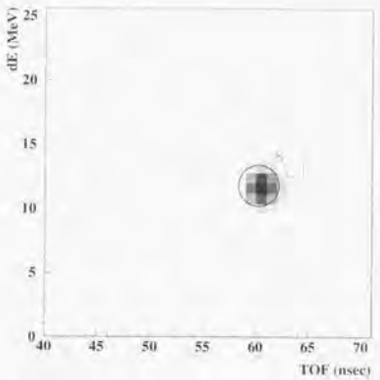

Figure 2.4: PI plot after inserting the achromatic degrader. Only ^{8}Li is selected and others are swept out.

	Magnetic Rigidity (Tm)			Momentum Acceptance (%)	Achromatic Degrader		Energy Degrader
nuclide	D1	D2	TQ3		wedge angle (mrad)	thickness (mg/cm^2)	thickness (mg/cm^2)
^{8}Li	2.884	2.642	0.769	± 2	4.46	816	1957
^{9}Be	2.405	2.227	0.769*	± 4	2.21	444	1130

Table 2.1: Parameter sets of the RIPS for the present experiment. The material of the degraders is aluminum. The achromatic degrader is at F1 and the energy degrader is at F2. (*This was missed to set, though the correct value is 0.684Tm.)

and are indicated on the PI plots. The density plot shows the relative intensity of each nuclear species, and the radius of the circle shown on the PI plot means the relative intensity estimated by INTENSITY-3.

Table 2.1 shows the tuning parameters of the RIPS to produce the ^{8}Li and ^{9}Be beams.

2.2.3 Low-energy beams

The ^{8}Li and ^{9}Be were separated from other nuclides by the RIPS and collected on the second focal plane (F2) of the RIPS, where a 7 mm-thick Al plate for ^{8}Li and a 4 mm-thick Al plate for ^{9}Be were placed to degrade the energies of ^{8}Li and ^{9}Be down to $2 \sim 4$ MeV/nucleon from $\sim$45 MeV/nucleon. The thickness of the Al plate was adjustable by rotating it. The energy-degraded ^{8}Li and ^{9}Be were selected and collected on the third focal plane (F3) with the specified rigidity by TQ3. Table 2.1 also gives the thickness of the energy degrader and the magnetic rigidities of TQ3. Finally, the low-energy ^{8}Li and ^{9}Be beams with an intensity of about $1 \sim 2$ kcps were injected into the MSTPC.

Figures 2.5 and 2.6 show the TOF-energy plots of the low-energy ^{8}Li and ^{9}Be beams. The TOF was measured by the F2- and F3-plastic scintillators and the energy was calculated. The horizontal axis is the TOF and the vertical axis is the energy measured by the F3 SSD which

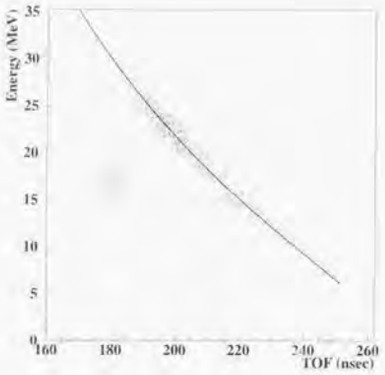

Figure 2.5: TOF-energy plot of the ^{8}Li beam at F3. The density plot shows the measured data and the solid curve shows the calculated data. The energy loss through the F3-plastic scintillator is corrected for.

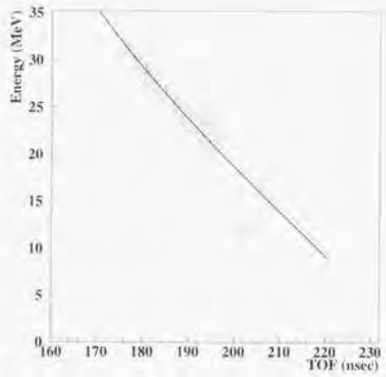

Figure 2.6: TOF-energy plot of the ^{9}Be beam at F3. The density plot shows the measured data and the solid curve shows the calculated data. The energy loss through the F3-plastic scintillator is corrected for.

was placed after the F3-plastic scintillator. The density plot and the solid curve indicate the measured data and the calculated value corrected for any energy loss through the F3-plastic scintillator, respectively. For calculating the energy loss through the F3-plastic scintillator, the thickness of the F3-plastic scintillator was determined to be consistent with the energy detected by the F3 SSD. The estimated average thickness was determined to be 63.3 μm, while the measured value was 68 μm near to the center of the active region.

Figure 2.7 shows a TOF-energy plot of the ^{8}Li beams injected into the MSTPC. The F3 SSD was installed in the MSTPC without the gases, and the energies after a thin kapton-film window (50 mm$^{\phi}$) of the MSTPC were also measured as a function of the TOF. The energy losses through the kapton film were also corrected for by energy-loss calculations. The estimated thickness of the film was 15.5 μm by assuming a kapton composed of $C_{22}H_{10}N_2O_4$ with a density of 1.42 g/cm^3, while the measured thickness was 12.5 μm and the uniformity was sufficiently good within 1.0 μm. Because the ingredients of kapton were not provided by the supplier, the difference between the estimated and measured thickness was due to uncertainty of the ingredients.

Although these plots show good agreement of the energy measured by the F3 SSD and the energy derived from the TOF and energy-loss calculation; the TOF-energy resolution was not good because the beam energy was widely spreaded by the F3-plastic scintillator. The dispersion was almost due to the non-uniformity in the thickness of the F3-plastic scintillator. The non-uniformity was up to $\pm 10 \sim 15$ μm and the energy dispersion resulted in 1.2 MeV (FWHM), while the uniformity was desired to be within ± 5 μm. The resolution of the TOF was within 1 nsec against the typical TOF, 150 nsec, and the uncertainty of the flight-path length was within 10 mm against the flight path, 5.299 m. The F3 SSD and read-out electronics were calibrated by an ^{241}Am α source (E_α = 5486 keV) and its energy resolution resulted in 2.4% (FWHM).

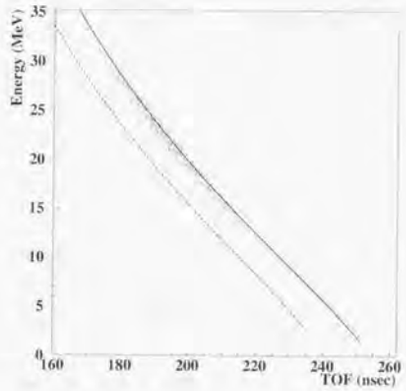

Figure 2.7: TOF-energy plot of the ^{8}Li beam injected into the MSTPC. The energy loss through the window film of the MSTPC is also corrected for. The dashed curve shows the ^{7}Li beam if it has the same velocity as ^{8}Li.

The linearity of the amplifiers and PH-ADC[4] were also examined by a research pulser, resulting in 0.9% (FWHM). The total dispersion due to the resolutions of the TOF, the flight-path length and the F3 SSD was within 0.5 MeV (FWHM).

2.2.4 Contamination in the beams

Although nuclides other than ^{8}Li or ^{9}Be were completely rejected by the isotopic separation at F2, contamination could be mixed after F2 due to a reaction in such thick materials as a plastic scintillator and an Al degrader. Because the neutron separation energy of ^{8}Li is small, 2.02 MeV, it seems that a breakup reaction is probable. The expected TOF-energy curve for the ^{7}Li, which is dissociated from the ^{8}Li by the F2 Al degrader or plastic scintillator, is shown in figure 2.7 as a dashed curve. By comparing the data, the estimated mixing ratio of ^{7}Li is below 0.25%. In addition, the Q value of the ^{7}Li(α,n)^{10}B reaction is -2.8 MeV, an endothermic reaction, and therefore ^{7}Li, if any, could not have any effect at the low-energy region.

Other contaminations could be rejected by the TOF, dE and tracking information, which was measured by the MSTPC. The analysis method is described in Chapter 5

2.3 Detector system

The MSTPC and neutron counters were used for detecting reactions and measuring particles. The MSTPC determined the reaction point and energy, and the neutron counters determined the neutron energy and angular distribution.

The details of the MSTPC and its electronics are described in Chapter 3.

[4]PH-ADC = Peak-Hold Analogue-to-Digital Converter.

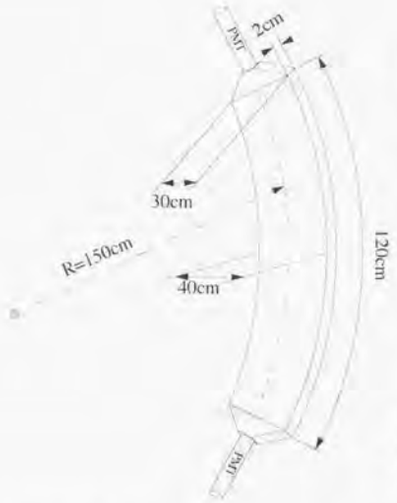

Figure 2.8: Illustration of the neutron counter.

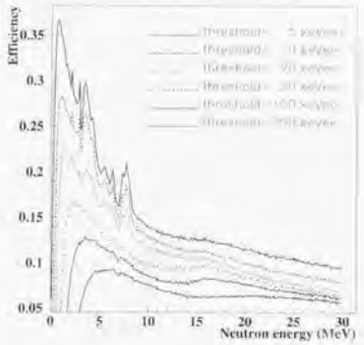

Figure 2.9: Results of an efficiency calculation. The horizontal axis is the neutron energy (MeV) and the vertical axis is the efficiency. Six cases of the threshold energy are shown. The threshold energy is in the unit of electron equivalent energy.

2.3.1 Neutron counters

The neutron counter comprised twelve sets of the plastic scintillator, BICRON BC408, each of which has the 120 cm long by 40 cm wide active area and are 2 cm thick. It has a barrel shape and a curvature center radius of 150 cm. Figure 2.8 shows a shape of the neutron counter.

The solid angle covered by one scintillator was 1.5% of 4π and the averaged intrinsic efficiency for a neutron at an energy region of $1.0 \sim 15$ MeV was about 10%, which was estimated by Monte-Carlo simulations coded by R. A. Cecil et al. [33]. This simulation code was optimized for the present neutron counter by M. Sasaki et al. [34], while considering the shape of the neutron counter and the measured light attenuation propagating through the plastic scintillator. The results of the simulation were fully examined by other experiments [35, 36], measuring β-delayed neutrons from ^{17}N.

Figure 2.9 shows the calculated efficiency of the neutron counter as a function of the neutron energy for various threshold energies. The threshold energy is shown in the unit of electron equivalent energy (keVee).

An energy calibration of the neutron counters was performed by measuring the Compton edge of the γ rays of ^{137}Cs (E_γ = 661 keV) and ^{133}Ba (E_γ = 356 keV). The pulse hight of PMT[5] measuring the gamma sources was nearly constant with $\pm$50 cm region from center of the neutron counter. In order to estimate the absolute efficiency, measurements with the fission source of ^{252}Cf were also performed. The threshold level was determined by measuring the fission source, and was set to be about 20 keVee, which corresponds to a neutron energy of 0.5 MeV. The details concerning the fission-source measurement are described in Appendix A.

[5]Photo-Multiplier Tube

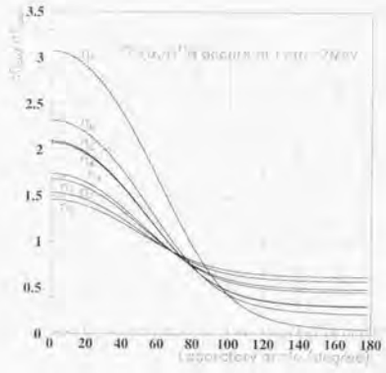

Figure 2.10: Solid-angle-transformation factor for the various final states of ^{11}B. The horizontal axis is the angle in the laboratory frame and the vertical axis is the factor of the solid-angle transformation. The reaction is assumed to occur at Ecm = 2 MeV.

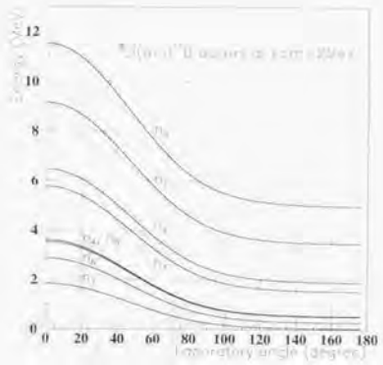

Figure 2.11: Neutron energies as the function of the laboratory angle for various final states of ^{11}B. The reaction is assumed to occur at Ecm = 2 MeV.

The neutron counters surrounded the MSTPC, symmetrically covering from 0 to 90 degrees, as shown in figure 2.1. The solid-angle-transformation factor from the center-of-mass system to the laboratory system is shown in figure 2.10, when a reaction occurs at a center-of-mass energy of 2.0 MeV. The angular distribution of the neutrons was forward peaked because of fast center-of-mass velocity of the colliding system. Figure 2.11 shows the neutron energies as a function of the laboratory angle when the reaction occurs at a center-of-mass energy of 2.0 MeV. The neutron energies in the forward direction, rather than 90 degrees, almost exceed the threshold of the neutron counter. Therefore, the present configuration of the neutron counter was reasonably efficient.

The PMTs were mounted on each side of the longitudinal direction of the plastic scintillator, and the position information of the hit along the longitudinal direction was derived from the time difference between two PMTs. The transverse position was determined by a scintillator which detected the neutrons. The position resolution of the longitudinal direction resulted in 4.5 cm (FWHM) and the position resolution of the transverse position was between 30 cm and 40 cm which was determined by the width of the neutron counter. Position calibrations were also performed by the γ sources.

The flight path of the neutron was derived from the reaction point determined by the MSTPC and the neutron position determined by the neutron barrel. The uncertainty of the flight path was estimated within 5.0 cm (FWHM) based on the position resolution of the neutron counter and the MSTPC. The position resolution of the MSTPC is described in Chapter 3.

Because the origin of the neutron TOF was the beam timing of the F3-plastic scintillator, the measured TOF (T_d) was a summation of the time (T_0) between the beam-passing time through F3 and the reaction-occurring time in the MSTPC, and the neutron-flying time (T_n). T_n is, of course, a true neutron TOF. In order to determine T_n, the offset time (T_0) was derived from

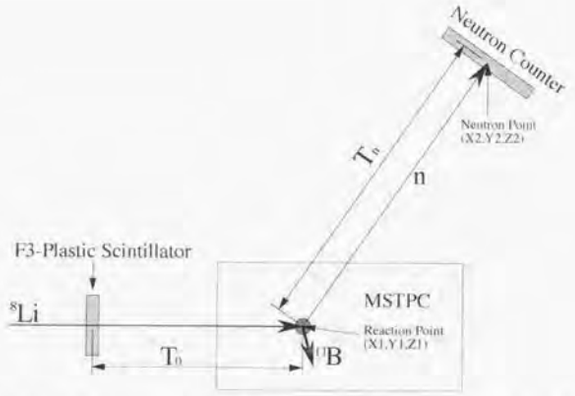

Figure 2.12: Method of the neutron-TOF determination. The measured time: $T_d = T_0 + T_n$, then $T_n = T_d - T_0$. The neutron-flight path: L=$\sqrt{(X2-X1)^2+(Y2-Y1)^2+(Z2-Z1)^2}$. The neutron velocity: $\beta_n = L/T_n$.

the reaction time, which was estimated by the reaction position determined by the MSTPC. Figure 2.12 shows how to determine the neutron TOF. The resolution of the neutron TOF was estimated to be within 5.0 nsec (FWHM) by the γ-flash peak width shown in figures 5.6 and 5.11.

2.3.2 MSTPC

The MSTPC was developed for experiments with low-energy unstable-nuclear beams. The MSTPC was designed based on the MUSIC-type [13, 23] detectors, which can measure the energy loss along the particle trajectories. The main advantage of the MUSIC-type detector is that the gas in the chamber works as both a detection medium and a gas target, a so-called active target, resulting in a high detection efficiency and a sufficient target thickness. Owing to these features of the MUSIC-type detector, the reactions induced by unstable-nucleus beams with limited intensities can be observed. In addition, the MSTPC has an advantage, which is the capability of the TPC (Time-Projection Chamber) employing a flash ADC to identify multiple-track events. The vertical position is determined by the drift time of the electrons in the gases, and the horizontal position is determined by employing the backgammon-type cathode pad.

^{8}Li beams were injected into the MSTPC filled with gases of ^{4}He admixed with 5% (10%)-isobutane gas at about 400 torr pressure. Although the iso-butane gas must be mixed for stable operation, they can contaminate the target. In order to estimate the background events by mixtures of ^{12}C and ^{1}H, 5% and 10% mixing ratios of the iso-butane gas were used.

For a beam passing through the gases and the occurrence of a nuclear reaction, the energy loss (dE/dx) changes rapidly according to the change in its Z number; thus, the energy and position where the reaction occurs are determined by detecting the dE/dx change with the MSTPC.

The details concerning the design, construction and performance study and applications of the MSTPC are described in Chapter 3.

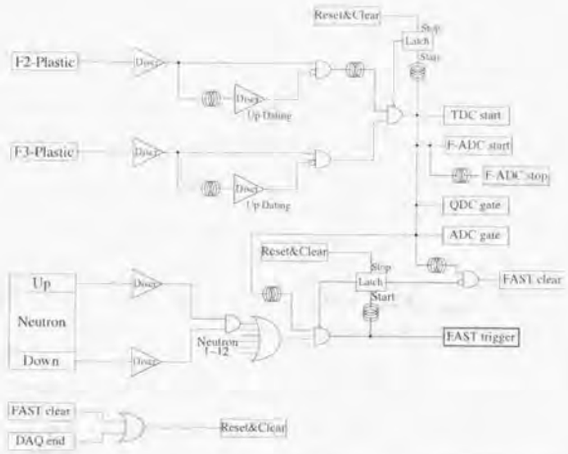

Figure 2.13: Diagram of the circuit. Only the main flow of the logic is illustrated. All of the analogue and timing signals of the detectors are recored by QDCs, ADCs and TDCs, respectively.

2.3.3 Circuits

Figure 2.13 shows a circuit diagram of the present experiment. The event trigger is produced by a beam trigger and a neutron trigger.

The beam trigger is generated when the following conditions are satisfied: coincidence of the signals of the F2-plastic scintillator and the F3-plastic scintillator within 140 $\sim$ 250 nsec of the F2-F3 TOF, and anti-coincidence with a pile-up signal having a period of 200 nsec for the timing signal of the F2-plastic scintillator and the F3-plastic scintillator. Here, pile-up rejection is important for a high counting-rate condition; if a particle passes another particle ahead, the TOF measurement will be confused. The acceleration cycle of the RRC for the present experiment was 12.35 MHz and a particle was produced every 81 nsec. Because this was shorter than the TOF between F2 and F3, typically 200 nsec, pile-ups could occur. Any pile-up beams could be also rejected by the MSTPC, since the MSTPC recorded any multiple-beam-track event.

The neutron trigger was generated when the following conditions were satisfied: coincidence with the signals of the beam trigger and any neutron counters within 300 nsec of the timing signal of the F3-plastic scintillator, which covers the estimated maximum T_d.

All analogue and timing signals from PMTs of the beam TOF counters and the neutron counters were recorded by QDCs[6], ADCs[7] and TDCs[8], respectively.

In the present experiment, the trigger rate was about 30 cps which included the true event and accidental-coincidence event. The beam intensity was about 1 kcps and the counting rate of

[6]Charge-to-Digital Converter.
[7]Analogue-to-Digital Converter.
[8]Time-to-Digital Converter.

State	Energy (MeV)	Γ_α (eV)	Γ_γ (eV)
11th	9.274	4×10^3	1.15 ± 0.16
10th	9.185	$1.6^{+1.5}_{-1.1}$	$0.17^{+0.06}_{-0.03}$
9th	8.920	0.0059 ± 0.0009	4.368 ± 0.021

Table 2.2: Table of the decay width [37]. It seems that Γ_γ is negligibly small compared to Γ_α or other particle-decay widths above the 10th excited state.

the neutron counter was about 3 kcps per one scintillator. Therefore, the accidental-coincidence rate was estimated to be about 20~30 cps, while the reaction-event rate was estimated to be about 0.001 cps. Although the trigger was mostly fired by the accidental-coincidence events, they could be rejected by off-line analysis.

2.4 ^{8}Li(α,n)^{11}B- and ^{9}Be(α,n)^{12}C-reaction properties

The ^{9}Be(α,n)^{12}C reaction has a similar property as that of the ^{8}Li(α,n)^{11}B reaction in terms of the Q value ($Q_{^8\mathrm{Li}(\alpha,n_0)^{11}\mathrm{B(gs)}} = 6.63$ MeV, $Q_{^9\mathrm{Be}(\alpha,n_0)^{12}\mathrm{C(gs)}} = 5.7$ MeV) and the level structure, as shown in figure 2.14.

Although the α-emission channel opens above 9th excited state of ^{11}B, the decay width of the 9th excited state is negligible small. $\Gamma_\alpha << \Gamma_\gamma$, as given in table 2.2 [37]. Therefore the states of ^{11}B from the ground state to 9th excited state are considered in the present experiment, simulation and analysis. In the case of ^{9}Be(α,n)^{12}C reaction, the 2nd excited state of ^{12}C decays to 3α with essentially 100% probability. Therefore only the ground state and 1st excited state of ^{12}C are considered.

Because ^{12}C has the simpler level structure than ^{11}B, it is useful to study the systematics of the present experimental procedure. The excitation functions of the cross section for each state of ^{12}C and the angular distributions of the ^{9}Be(α,n)^{12}C reaction were well measured [24, 25, 26, 27, 28]. Hence, the ^{9}Be(α,n)^{12}C reaction should have given us a good calibration of the present experimental procedures.

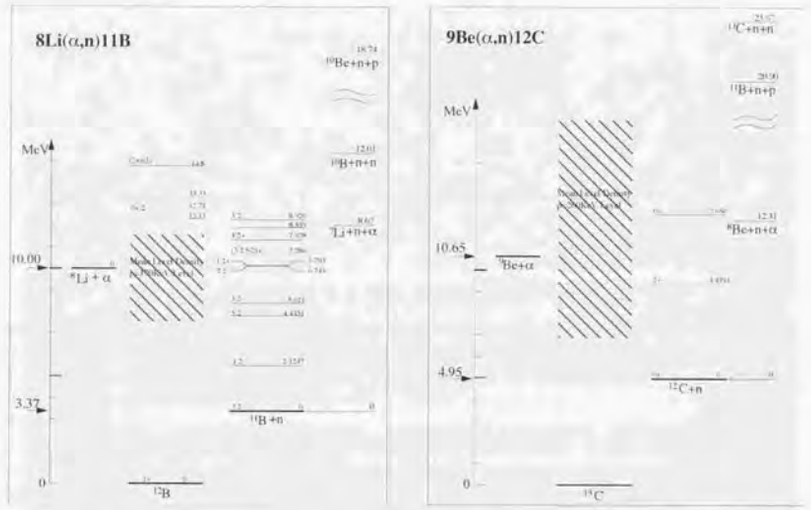

Figure 2.14: Level schemes and properties of the ^{8}Li(α,n)^{11}B and ^{9}Be(α,n)^{12}C reactions. The vertical axis shows the reaction energy of the entrance channel and the excitation energies of the intermediate compound state or exit channels in unit of MeV. The ground state of intermediate compound nuclei is set to be 0 MeV.

Chapter 3

Design and Construction of Multiple Sampling and Tracking Proportional Chamber -MSTPC-

The MSTPC was designed for the purpose of low-energy RI beam experiments. The main features of the MSTPC are three-dimensional-tracking capability and dE/dx multiple sampling of multiple particles. The details are described in this chapter.

3.1 Design of the MSTPC

The MSTPC was designed in order to obtain a three-dimensional-tracking capability of multiple particles for the clear identification of the event type, and also to obtain fine-pitch sampling of the stopping power (dE/dx) for an accurate determination of the reaction point.

Figure 3.1 shows a photograph of the MSTPC. Figure 3.2 shows a cross-sectional view of the MSTPC. The MSTPC consists of a field cage and 64 backgammon-type cathode-pad cells with anode and grid wires. The MSTPC is installed in a vacuum chamber made of aluminum and operated at a pressure of a few hundred torr or less.

Figure 3.3 shows the principle of the MSTPC. The electrons ionized from the gas molecules by incident particles passing through the gases drift to grid wires due to a uniform electric field supplied by the field cage. The electrons passing through the grid wires are amplified by the anode wire and the induced charges are detected by the cathode pads. The cathode-pad cells with their anode wires are aligned perpendicular to the beam direction so as to allow multiple sampling of dE/dx of the particle along the track. The vertical position is determined by the drift time, and the horizontal position is obtained by measuring the induced charges on both sides of the backgammon-type pads. The signal from the cathode pad is read out by a charge-sensitive preamplifier (Pre-AMP), a shaper amplifier (S-AMP) and a flash-ADC (F-ADC). Sampling the signals by the F-ADC as time-sequential data, the MSTPC can perform three-dimensional tracking for multiple particles, like the time-projection chamber (TPC).

3.1.1 Field cage

The field cage has a 70 cm long, 15 cm high, and 20 cm wide active area. The vertical position of the trajectory is determined by the electron-drift time in the field cage. The electric field with a simple configuration of the field wires may not be uniform, which is undesirable for determining

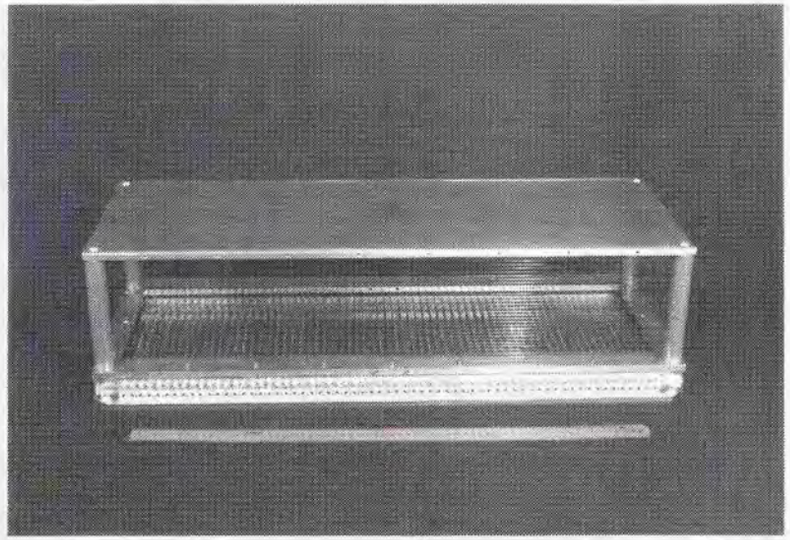

Figure 3.1: Photograph of the MSTPC. A 50 cm scale is also displayed.

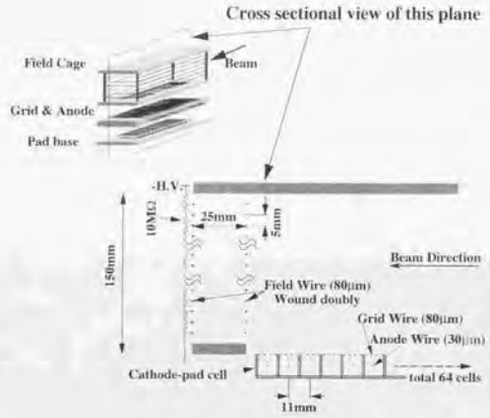

Figure 3.2: Cross-sectional view of the MSTPC. The MSTPC has three components: a field cage for providing a uniform vertical electric field, an anode wire for multiplying the charges and cathode-pad cells for detecting any induced charge.

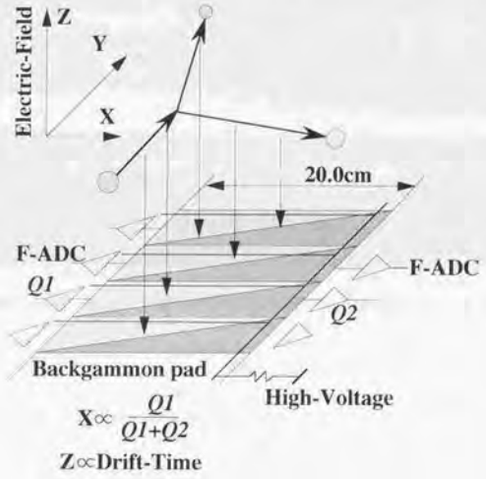

Figure 3.3: Illustration of how to measure three-dimensional trajectories and energy loss along with these trajectories for reactions involving multiple particles. For a better view, the grid wires are not drawn.

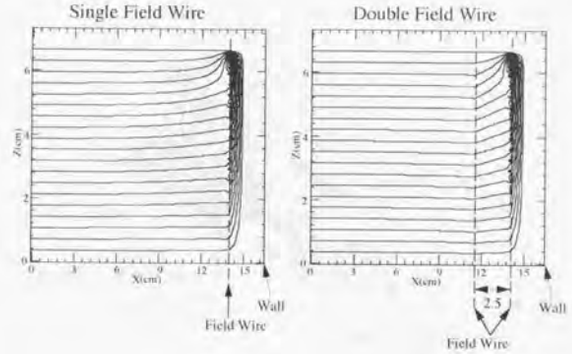

Figure 3.4: Field calculations for the drift space. The x-axis and z-axis are defined in figure 3.3. The solid lines show the equipotential surfaces. The right (doubly wound) has better uniformity than the left (singly wound). The wall of the vacuum chamber is x = 15 cm and grounded.

the vertical position, because the walls of the vacuum chamber are very close to the field cage. Thus, the field wires, which are 80 μm$^{\phi}$ Cu-Be wires, are wound doubly spaced by 5 mm to obtain a better uniformity of the drift field. Figure 3.4 shows the calculated equipotential surfaces of the field cage, comparing the two cases of field wire configuration. The left side shows the singly-wound case and the right side shows the doubly-wound case. Uniformity of the latter is better than that of the former.

The position resolution of the vertical (drift) direction depends on the drift velocity of the gases; a typical value is around 1 mm (FWHM).

3.1.2 Cathode pads, anode and grid wires

In the case of a low-energy nuclear reaction, the multiplicity of charged particles in the final state is at most two or three. Thus, the highly segmented cathode pad used in an ordinary TPC for high-energy experiments is not needed. The cathode pad of the MSTPC is segmented only in the transverse direction against the beam direction.

At first, a resistive-ceramic cathode pad was installed for horizontal position tracking in the prototype MSTPC [38, 39], and was tested. Although the position resolution and linearity were as good as the backgammon-type cathode-pad, the time difference, which depends on the horizontal position between both sides of the cathode pad, was not small (max 1 μsec). This time difference, which may be due to the diffusion time of the charges in the resistive ceramic, is comparable to the drift time in the gas, and it is very confusing to determine each drift time for multiple tracking.

In order to avoid this problem, the backgammon-type cathode-pad, which can be made of a good conductor and can be used for a position determination, is employed.

Figure 3.5 shows a schematic view of the backgammon-type [40] cathode-pad cell. The MSTPC has 64 cathode-pad cells, and each cathode-pad cell is 1 cm long, 1 cm high, and 20 cm wide. The cathode-pad cell has an anode wire (30 μm$^{\phi}$ Cu-Be) and 2.5 mm spaced grid wires

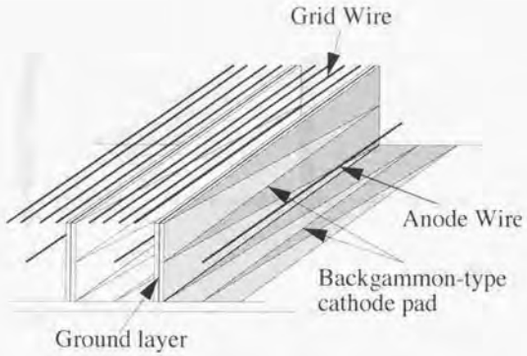

Figure 3.5: Schematic view of the backgammon-type cathode-pad cell. The cathode pads surround the anode wire. The ground layer is placed between the cathode-pad layers to prevent cross talk.

($80\ \mu m^{\phi}$ Cu-Be).

The backgammon-type cathode pad has a specific geometry pattern so as to divide the charges for encoding the position information. The charges induced on the cathode pad are read out from the left and right sides of the cathode pad and the horizontal position of the trajectory is determined by the ratio of the charges from both sides. The geometric pattern of the cathode pad was designed on a PC board. For protection against corrosion, the surface of the cathode pad was electro-plated with gold. In order to prevent cross talk between adjacent anode wires, three planes of cathode pads surround the anode wire, and the ground layer is put between the cathode-pad patterns. In addition, by covering the solid angle of about 3/4 around the anode wire, the read-out charges are increased, and hence the position resolution may be improved. By increasing the read-out charge, the acceptable beam intensity increases, because the operating gas multiplication can be decreased. Figure 3.6 shows the position resolution of a prototype of the backgammon-type cathode pad, measured with a collimated α source (^{241}Am). The three-plane data show that it improves the position resolution, and makes the resolution nearly constant along the anode wire, as opposed to the one-plane or two-plane data. Figure 3.7 shows the print pattern of the present backgammon cathode pad.

3.2 Electronics and data-acquisition system

Figure 3.8 shows a diagram of the MSTPC readout system. The induced charges on the cathode pad are integrated and converted to a voltage by a factor of about 1 V/pC by the Pre-AMP.

The output signal from the Pre-AMP is divided into three parts. The first signal is discriminated and used as one of the trigger signals. The second signal is shaped to a semi-Gaussian by the S-AMP and sampled by the F-ADC. The third signal is shaped to a semi-Gaussian by the S-AMP and digitized by a peak-hold ADC (PH-ADC).

The data processed by the ADCs are collected by a TKO [41] and CAMAC system. The

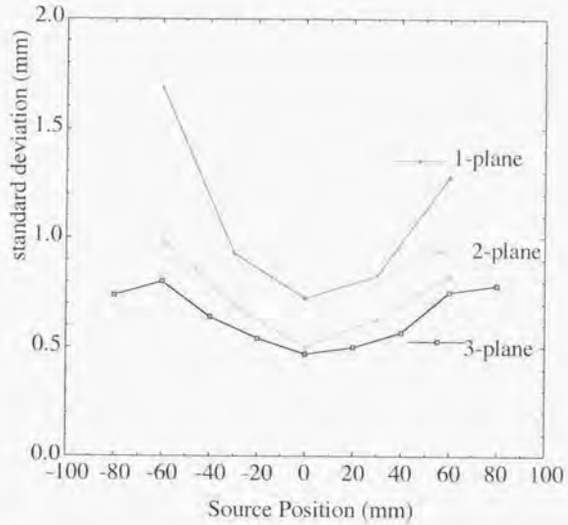

Figure 3.6: Position resolution of the prototype-backgammon-type cathode pad. The position resolutions were measured by one plane, two planes facing each other and three planes.

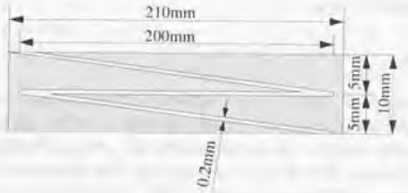

Figure 3.7: Backgammon pattern for the present cathode pad.

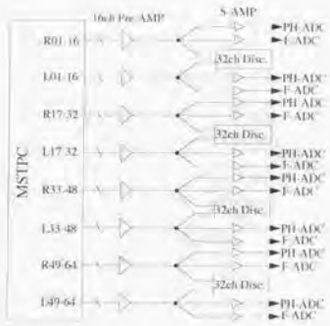

Figure 3.8: Diagram of the MSTPC readout system. The signals from the MSTPC are read out by the Pre-AMPs and divided. The divided signals are processed by the S-AMPs and ADC's. The discriminated signals are used for a trigger. The R01-16 means the signals from the right side of the cathode-pad number from 1 to 16 and the L01-16 means the signals from the left side of those.

TKO and CAMAC interfaces are installed in the VME crate. A data-acquisition (DAQ)-front-end computer is also installed in the same VME crate and connected to an on-line monitor computer by the Ethernet.

3.2.1 Charge sensitive preamplifier

The MSTPC has 64 cathode-pad cells to be read out from both sides of each cathode pad; thus, 128 channel Pre-AMPs are required. For handling the Pre-AMPs easily, a 16-channel Pre-AMP board was designed. Each Pre-AMP has a 1pF feedback capacitor and a 1 μsec time constant to shorten the tail of the signal so as to minimize any pile-up of the signal. Eight Pre-AMP boards were mounted outside of the vacuum chamber and shielded by an aluminum chassis. The output signals are divided into 3 parts and fed to a discriminator, the S-AMP for the F-ADC and S-AMP for the PH-ADC, respectively.

3.2.2 Discriminator

In order to create a reaction trigger, a discriminator was incorporated. For example, when a fusion-like reaction occurs, the nuclear charge greatly increases and dE/dx changes rapidly. Then, a fusion-like event trigger can be generated by setting the discriminator level above dE/dx for the incident beam. The discriminator circuit has 32-channel inputs; the 16 channels are for the left side of the cathode pads and the other 16 channels are for the right side of the cathode pads, with a common threshold for 32 channels. The output signals of the discriminator are the fast NIM-level logic signal, having a non-updating 200 nsec width, for 32 channels, and 16 coincidence signals of both sides of one cathode pad. In addition, the multiplicity signals, the multiplicity of the 16 left-side channels, the 16 right-side channels and the 16 channel coincidences of both sides are available. The multiplicity output of the other discriminator

modules can be connected by a daisy-chain configuration.

In the measurement of a fusion reaction, the right-side signal and the left-side signal are discriminated separately and an event trigger is fired by the coincidence of those, in order to select not only the dE/dx change, but also the reaction point, which should localize around the center, because the fusion reaction causes large dE/dx changes and the fusion product runs nearly forward, as opposed to other scattering reactions which brings about dE/dx changes with its trajectory change.

On the other hand, the anode-wire signals are discriminated instead of the summed signals of the right and left-side signals of the cathode pad, when the event trigger is required to be fired due to the dE/dx changes independent of the position information. The anode-wire-signal discriminating system is available as required, although it was not used in the present experiment.

3.2.3 Shaper amplifier and flash ADC

The MSTPC employs a F-ADC module which was developed for the TPC at KEK and improved for the present use. The present F-ADC module has 8-channel S-AMPs to shape the signal into a semi-Gaussian form with a 250 nsec FWHM, F-ADCs which sample at 40 MHz and convert an analogue input to 8-bit digital data, and 1 kbyte buffer memories. The sampling rate is variable up to 70 MHz. The specific energy resolution of the electric circuit was measured by feeding a test signal into the Pre-AMP and sampled by the F-ADC module; it was found to be within the lowest 2 bits (FWHM) [42].

3.2.4 Shaper amplifier and peak hold ADC

In some cases, the dynamic range of the 8-bit F-ADC is not wide enough to measure the large dE/dx change of a fusion-like event; however, the wide dynamic-range F-ADC is very expensive. In order to solve the cost problem, a 12-bit PH-ADC module, which is a popular CAMAC module, and a S-AMP module, which is a popular NIM module, can be employed in parallel to the F-ADC read out, as shown in figure 3.8.

3.2.5 Data-acquisition system

Figure 3.9 shows a schematic view of the DAQ system. This system consists of F-ADC modules on a TKO bus, CAMAC modules, interface modules between the the TKO and CAMAC to the VME, and an HP9000 board computer on the VME bus. The interface module of the TKO side is a SCH (Super Control Head), which has some sequence programs. The interface module of the VME side is a SMP (Super Memory Partner), which has the function of zero suppression and 4 Mbyte double buffers. The 16 modules of the F-ADC are segmented into 4 blocks, and 4 sets of the SCH and SMP pairs are used to take data in parallel. In this system, transferred data from the F-ADCs are maximum at 128 kbytes/event. By utilizing the SMP, data from the SMP to the front-end computer are reduced to about 20 kbytes/event. The HP9000 board computer is operated in real time UNIX, HP-RT, and has high performance to collect massive data [43]. To control this system, a UNIDAQ system [44] was installed on both computers. A DDS2-DAT drive is connected to the board computer and the data are recorded on the DAT. The data-acquisition rate is up to 20 events/sec by the present system with typically 20 kbytes per event [42].

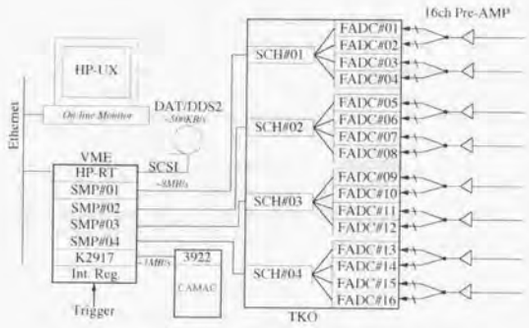

Figure 3.9: Schematic view of the DAQ system.

3.3 Detection efficiency

Figure 3.10 shows the detection efficiencies of the cathode pads, which was measured with ^{8}Li beam and 10%-isobutane-mixed gas. They are calculated as follows: when both the first (entrance) and 48th (exit) pads detect a particle, whether the other pads can detect the particle or not. In the case of 5%-isobutane-mixed gas or ^{9}Be beam, the same efficiency is obtained.

The lowest efficiency of one pad is above 0.998; then, the efficiency of all pads is above $0.998^{48} = 0.91$. This is not problem for practical use if one of the pads does not fire, because it can be complemented by both-side pad of it by analysis. Therefore, the detection efficiency of the MSTPC is essentially 100%.

3.4 Measurement of the ^{8}Li(α,n)^{11}B and ^{9}Be(α,n)^{12}C reactions

In the present experiment, 48 channels in the upper stream out of all cathode pads were used, because the electronics were ready for only 48 channels. In this experiment, the event trigger was generated by the coincidence between the beam counter and the neutron counter, whereas the discriminator module for MSTPC was not incorporated.

The MSTPC was filled with the ^{4}He gas with an admixture of the 10%-iso-butane gas or the 5%-iso-butane gas at 400 torr pressure. A gas-flow system was not used, because the vacuum chamber was sufficiently evacuated and the gas leakage was found to be adequately small ($< 10^{-3}$ torr/day) for one day of operation. However, the gas was refilled every half day for safe operation.

The anode and field voltages are given in table 3.1. In order to keep the pulse height of the cathode pad nearly constant for various beam species and gas combinations, the anode voltage was tuned. The field voltage was set to be -1200 V, where the drift velocities of the electron were about 1.4 cm/μsec for a 10%-isobutane-mixed gas, and about 1.3 cm/μsec for a 5%-isobutane-mixed gas.

The vacuum chamber had flanges with 100 μm-aluminized-mylar film for a neutron window.

Figure 3.11 shows a three-dimensional plot of the averaged dE/dx for ^{8}Li beams with various

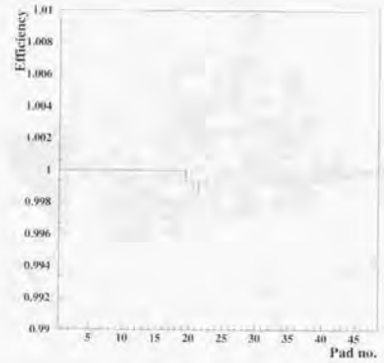

Figure 3.10: Efficiency of the MSTPC. The horizontal axis is the pad number; the beam runs from left to right. The vertical axis is the efficiency. It is measured with the ^{8}Li beam and 10%-isobutane-mixed gas. The number of injected beams is ten million.

Beam	Gas	Anode (V)	Field (V/cm/atm)
^{8}Li	^{4}He+10% iso-butane	+780	-190
^{8}Li	^{4}He+5% iso-butane	+750	-190
^{9}Be	^{4}He+10% iso-butane	+730	-190
^{9}Be	^{4}He+5% iso-butane	+710	-190

Table 3.1: Table of the high voltages. The anode voltage is selected to make a cathode-pad signal constant. The field voltage is set to be -1200 V$= -190$ V/cm/atm.

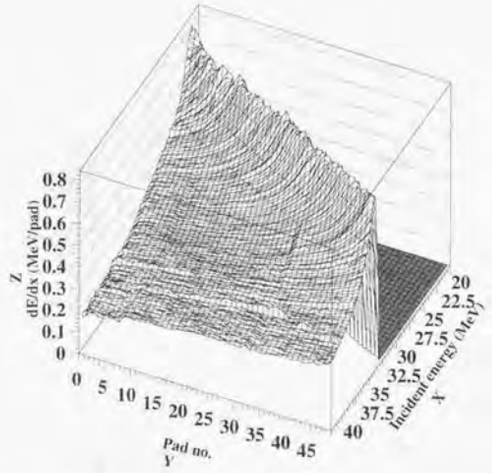

Figure 3.11: Three-dimensional plot of the Bragg curve of the ^{8}Li with various incident energies.

energies. The x-axis represents the energies of incident ^{8}Li beams. The y-axis represents the cathode-pad numbers. The z-axis represents dE/dx; the dE/dx values measured by the cathode pads were calibrated to fit an energy-loss calculation by the computer code [45].

Figure 3.12 shows an example of the Bragg curve of the ^{8}Li beam, which is a slice of figure 3.11 at an incident energy of 27 MeV and 32 MeV. The error bar shows the standard deviation of dE/dx, which is mainly due to energy straggling and energy uncertainty owing to the non-uniformity of the F3-plastic scintillator.

Figure 3.13 shows a typical event of the ^{8}Li(α,n)^{11}B reaction. The horizontal axis represents the cathode-pad numbers. The vertical axis represents dE/dx. The reaction position is determined by a sudden change of dE/dx from the Bragg curve, and the reaction energy is determined by calculating the incident energy and the energy losses through the gas.

In addition to the energy losses, trajectory information is obtained by the MSTPC. Figures 3.14 and 3.15 show the typical event of the ^{8}Li(α,n)α^7Li reaction. The former figure shows one example of the raw data of the F-ADC. The right-side-pad signal and the left-side-pad signal are shown. The dE/dx and position values are derived from them and shown in the latter figure. The horizontal axis and vertical axis represent the cathode-pad numbers and the horizontal or vertical position, respectively. The radius of the circle along the tracks is proportional to dE/dx. The reaction position is determined by calculating the cross point of two or three tracks.

The energy of the incident particles at the reaction point is determined by the MSTPC, and the energy and angular distribution of the neutrons are determined by the neutron detector, which is segmented and read out from both sides by PMTs to obtain position information. Then, the invariant mass of the reaction can be calculated by assuming that the target is an α particle. If the invariant mass satisfies the event gate corresponding to the ^{11}B mass, the event

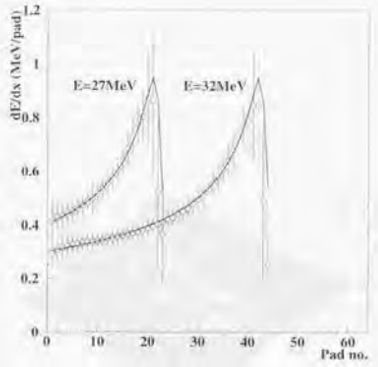

Figure 3.12: Bragg curves generated by a slice of figure 3.11 at incident energies of 27.0 ± 0.1 MeV and 32.0 ± 0.1 MeV. The solid curves represent the calculated stopping power (dE/dx).

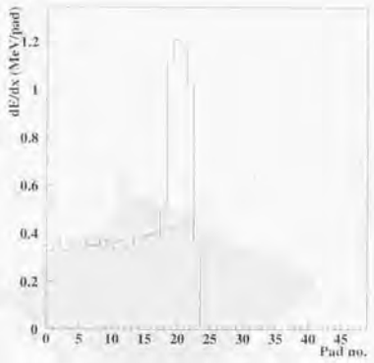

Figure 3.13: Typical event of the ^{8}Li(α,n)^{11}B reaction. The solid curve shows the reaction event and the dashed line shows the Bragg curve of the ^{8}Li. When the ^{8}Li beam reacts with the α-particle target, dE/dx changes suddenly.

is selected as the reaction event.

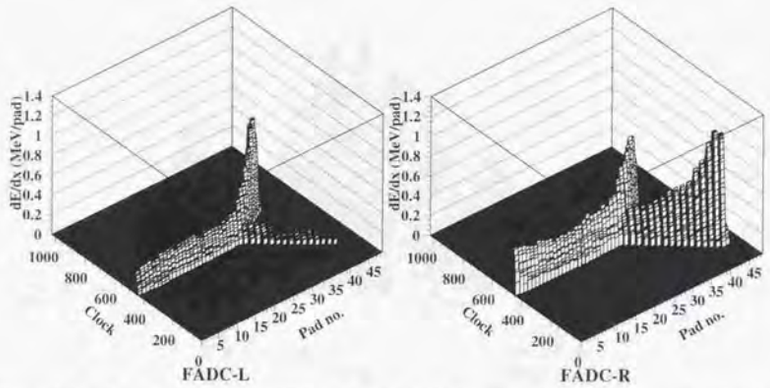

Figure 3.14: Raw data of the F-ADCs. The left-side figure is the left-side signals, and the right-side figure is the right-side signals. The clock axis means the sampling-clock count. One clock equals to 25 nsec.

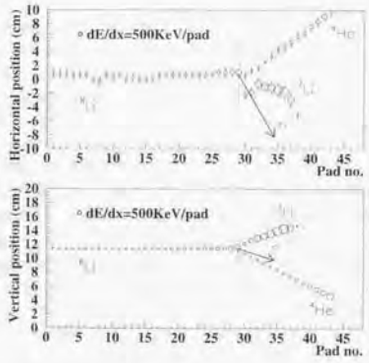

Figure 3.15: Typical event of the ^{8}Li(α,n)α^7Li reaction. The ^{8}Li beam reacts with the α-particle target and the α particle, ^{7}Li and the neutron are emitted. The neutron is detected by the neutron detector at the direction of the arrow. The error bars mean uncertainty of the position determination.

Chapter 4

Simulations and Estimations

Computer-simulation codes were written for estimating the efficiencies of the detection system and analysis procedure. In addition, in order to predict the response functions, simulations were performed. Background events were also simulated in order to estimate their effects.

4.1 Simulation procedure

The main factors which determine the efficiencies are the detection efficiencies of the detectors, the solid angle covered by the detectors, and the analysis efficiency.

The detection efficiencies of the neutron counters are discussed in Appendix A. The simulation method concerning the neutron counter has a systematic error of within 10%, which was not considered in the presently discussed simulation for simplification.

The detection efficiency of the MSTPC is shown in figure 3.10. As described in Section 3.3, the detection efficiency of the MSTPC is essentially 100%. While the solid angle for detecting a reaction by the MSTPC is essentially 100%, that for neutrons by the neutron counter varies according to the length between the reaction position and the neutron counter; hence, the solid angles must be calculated by a computer simulation which includes the detector setup and its geometries.

Furthermore, the efficiency of the analysis process must be considered. In order to estimate the overall efficiencies, which include the detection efficiencies, the solid angles and the analysis efficiency, the event data are generated as just the same structure of a real event and are analyzed by the same analysis programs. The event-generation program simulates an event in the following way:

1. Event simulation:

   Step 1. The ^{8}Li-beam energy, momentum and injection point are set. Here the beam profiles derived from the measured data are used.

   Step 2. The reaction-occurring energy is selected.

   Step 3. The excited state of ^{11}B is selected.

   Step 4. The ^{8}Li-beam-energy losses, energy stragglings and multiple scatterings through the F3-plastic scintillator are calculated. The thickness of the F3-plastic scintillator is distributed at random within the measured thickness non-uniformity.

   Step 5. The ^{8}Li-beam-energy losses, energy stragglings and multiple scatterings through the MSTPC-window film are calculated.

Step 6. The ^{8}Li-beam-energy losses, energy stragglings and multiple scatterings passing through the gases are calculated step by step, until the beam energy decreases to be equal to or lower than the reaction energy selected by [**Step 2**].

Step 7. The kinematics are calculated; the neutron energy and momentum are determined by assuming an isotropic angular distribution in the center-of mass system, and the ^{11}B energy and momentum are determined. ^{11}B has the excitation energy selected by [**Step 3**].

Step 8. A neutron passes to the neutron counters. Whether a neutron is detected or not is determined based on the geometry and the detection efficiency of the neutron counter. The detection probability is determined according to the function of the neutron energy and the efficiency shown in figure A.2.

Step 9. The excited ^{11}B decays to the ground state by single-gamma emission with a spherical-angular distribution in the rest-mass system of the excited ^{11}B. A cascade-gamma decay is not considered, because the kinematical effect of γ ray emission is negligibly small.

Step 10. The ^{11}B(gs)-energy losses, energy stragglings and multiple scatterings passing through the gases are calculated, until the ^{11}B(gs) stops inside, or escapes from, the active region of the MSTPC.

2. DAQ simulation:

Step 1. The TOF values of the ^{8}Li beam measured by the F2 and F3-plastic scintillators are digitized by the TDCs and the QDCs with the resolution determined by the experiment data.

Step 2. The TOF value of the neutron measured by the neutron counter is digitized by the TDCs and the QDCs with the resolution determined by the experiment data.

Step 3. The energy losses per pad and the electron-drift times are sampled by the flash ADCs with noise signals determined by the experiment data. The electron-diffusion effect is included in the position resolution.

Step 4. All data are recorded in a file having the same data structure as the on-line DAQ.

These simulation processes are performed for various states from the ground state to the 9th excited state of ^{11}B with the 5% and 10%-isobutane-mixed gas; the data sets are analyzed by the same computer codes as those are used for the present analysis. The details concerning the analysis are described in Chapter 5. For the ^{9}Be(α,n)^{12}C reaction, the same procedures are performed. In the case of ^{12}C, the ground state and 1st excited state are considered. Because angular-distribution data are available for the ^{9}Be(α,n)^{12}C reaction, simulations are performed for two case: one assumes a spherical distribution, and the other assumes the angular distribution derived from the reference data [24, 25, 26, 27, 28]. Since ^{11}B and ^{12}C decay by particle emission above the 10th excited state of ^{11}B and the 2nd excited state of ^{12}C, the simulations were performed for below the 9th excited state of ^{11}B and the 1st excited state of ^{12}C.

The number of generated events is about 10,000 per one state of ^{11}B and ^{12}C, which is much larger than the experimental data. By these procedures, the overall efficiencies for each individual excited state are determined.

	Efficiency	Systematic Error
$\varepsilon_{neutron}$	$10 \sim 20\%$	$\pm 1\%$
$\Delta\Omega_{neutron}$	$\sim 20\%$ of 4π	
ε_{MSTPC}	$\sim 100\%$	
$\Delta\Omega_{MSTPC}$	$\sim 100\%$ of 4π	
$\varepsilon_{analysis}$	75%	$\pm 5\%$
$\varepsilon_{overall}$	$1 \sim 2\%$	$\pm 0.05\%$

Table 4.1: Summary of the efficiencies. A rough estimation of the efficiency with the systematic error is given.

4.2 Overall efficiencies

The absolute cross sections are derived by correcting the analyzed data using the overall efficiencies, which include intrinsic detection efficiencies, geometries of the detectors, and analysis efficiency. They are discussed in this section for the relevant cases.

Here, the overall efficiency, $\varepsilon_{overall}$, is defined as a function of the reaction energy, Ecm, and the excitation energy of ^{11}B, Ex, and is described as

$$\varepsilon_{overall}(Ecm, Ex) = \varepsilon_{neutron} \times \Delta\Omega_{neutron} \times \varepsilon_{MSTPC} \times \Delta\Omega_{MSTPC} \times \varepsilon_{analysis} \ , \qquad (4.1)$$

where $\varepsilon_{neutron}$ is the detection efficiency of the neutron counter, $\Delta\Omega_{neutron}$ is the solid angle covered by the neutron counters, ε_{MSTPC} is the detection efficiency of the MSTPC, and $\Delta\Omega_{MSTPC}$ is the solid angle covered by the MSTPC, and $\varepsilon_{analysis}$ is the analysis efficiency. A rough estimation of these factors is summarized in table 4.1. The precise estimation is described in following sections.

4.2.1 ^{8}Li(α,n)^{11}B reaction

Figures 4.1 and 4.2 show the efficiencies of the ^{8}Li(α,n)^{11}B reaction. The higher is the excitation energy of ^{11}B, the higher is the efficiency, because the lower is the neutron energy, the higher is the detection efficiency of neutron counter. The angular distribution is assumed to be isotropic, since there is no reliable data concerning the level property of the intermediate states of ^{12}B*. The reaction events occurring near the top of the Bragg curve can not be analyzed due to the range straggling, so that the cut off energy of analysis is set to be the center-of-mass energy of 1.5 MeV.

4.2.2 ^{9}Be(α,n)^{12}C reaction

Figure 4.3 shows the efficiencies of the ^{9}Be(α,n)^{12}C reaction. The difference between the result for the case of an isotropic angular distribution and that for the case of using the measured angular distribution is 5~10%. This suggests that the results of the ^{8}Li(α,n)^{11}B reaction have a 5~10% systematic error, since an isotropic distribution was assumed in their analyses. The cut off energy of analysis is set to be the center-of-mass energy of 2.0 MeV for this case.

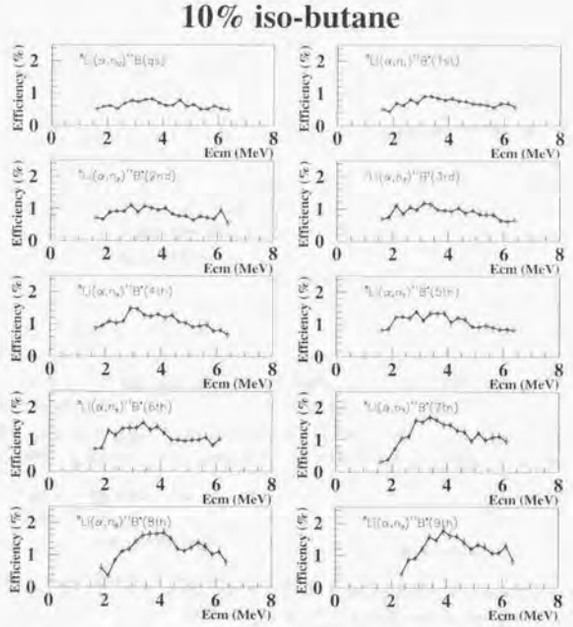

Figure 4.1: Simulated overall efficiencies for the ^{8}Li(α,n)^{11}B reaction in the case of the 10% isobutane-mixed gas. The horizontal axis shows the center-of-mass energy and the vertical axis shows the overall efficiency. The efficiencies are calculated for various final states of ^{11}B. The error bar represents the statistical error only. The solid line is drawn to guide the eye.

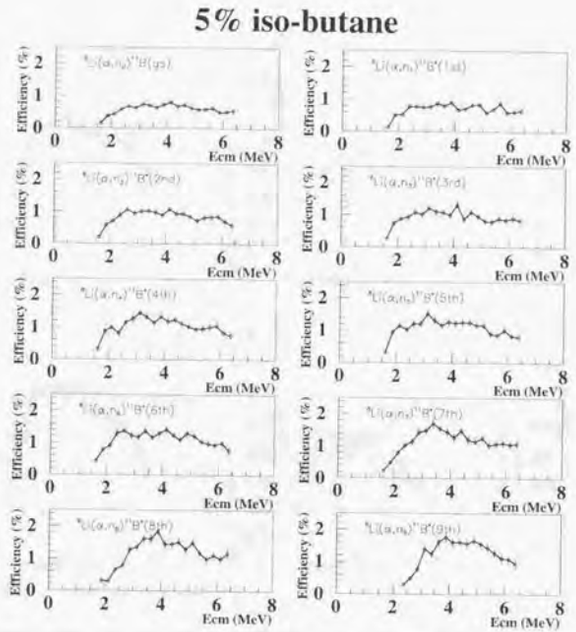

Figure 4.2: Simulated overall efficiencies for the ^{8}Li(α,n)^{11}B reaction in the case of the 5% isobutane-mixed gas. The horizontal axis shows the center-of-mass energy and the vertical axis shows the overall efficiency. The efficiencies are calculated for various final states of ^{11}B. The error bar represents the statistical error only. The solid line is drawn to guide the eye.

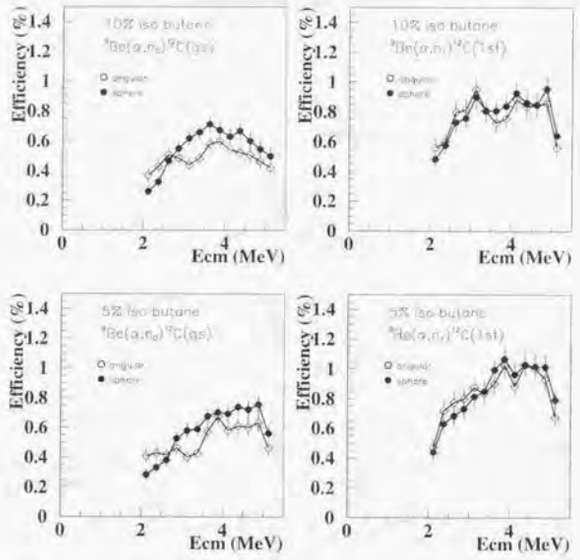

Figure 4.3: Simulated overall efficiencies for the ^{9}Be(α,n)^{12}C reaction. The upper figures show the case for the 10%-isobutane-mixed gas and the lower figures show the case for the 5%-isobutane-mixed gas. The left-side figures show the case of decay to the ground state and the right-side figures show the case of decay to the 1st excited state. The white circles show the simulation with the angular distribution given by the references and the black circles show the simulations with isotropic angular distributions at the center-of-mass system. The error bar represents the statistical error only. The solid line is drawn to guide the eye.

4.3 Response function

Because the statistics of the present experiment are not very sufficient to separate the transitions to the individual levels of ^{11}B, the response functions of the excitation-energy spectrum of ^{11}B are used to estimate the cross section to the relevant levels. The response function is obtained by analyzing the simulated data.

4.3.1 ^{8}Li(α,n)^{11}B reaction

The data analysis is performed for the simulation data of 10,000 events per one state of ^{11}B, and the peak spectra of the various ^{11}B levels is derived by integrating the events from 2 MeV to 7 MeV in the center-of-mass system. The peak spectrum is fitted with the Gaussians whose center values correspond to the ^{11}B levels, and the standard deviations are derived.

Figure 4.4 shows the response functions of the various states of ^{11}B. The peak width is narrower at a higher excitation-energy state, because the TOF resolution becomes better due to the lower neutron energy and the longer neutron TOF.

At the stage of designing the experiment, it was presumed that the thickness of the F3-plastic scintillator would be 100 μm and its uniformity would be within 10 μm, 10% for 100 μm; however, the uniformity of the present scintillator is actually 15 μm for 65 μm thickness, as described in Subsection 2.2.3. Therefore, the presently mentioned resolutions of the level separation are not as good as assumed, due to the uncertainty of the beam energy. Figure 4.5 shows the expected excitation-energy spectrum of ^{11}B with the 10%-uniform scintillator. The ground state and 1st excited state are separable, in contrast to figure 4.4.

4.3.2 ^{9}Be(α,n)^{12}C reaction

Figure 4.6 shows the response functions for the simulated excitation-energy spectrum of ^{12}C, which is obtained by integrating the center-of-mass energy from 2 to 5.2 MeV. Although they take into account the angular distributions of the neutrons derived from reference data, they are not changed depending on the angular distribution. The standard deviations of the excited states are determined by fitting the spectrum with the Gaussians.

4.4 Background estimation

The background events are also simulated by the same procedure. The possible background events are in three categories; i) reaction with ^{12}C, ii) reaction with ^{1}H, and iii) breakup reaction with ^{4}He. The ^{12}C and ^{1}H nuclei are the components of the iso-butane gas mixed with ^{4}He gas.

4.4.1 Reaction with ^{12}C and ^{1}H

Because many final states of a reaction with ^{12}C are possible due to their large Q values, for example ^{8}Li+^{12}C→n+^{19}F+14 MeV and ^{9}Be+^{12}C→n+^{20}Ne+10 MeV, it is difficult to simulate all possible final states. Therefore, in order to estimate the effects of ^{12}C and ^{1}H targets, the two mixing-ratio gases are used. If a pure ^{4}He target could be used, it would be better in terms of the background; however, a pure ^{4}He target can not be used for the present experiment due to unstable operation.

Comparing the analyzed data for the 5%-isobutane-mixed gas and that for the 10%-isobutane-mixed gas, shown in figures 5.10, 5.14 and 5.15, it seems that the reactions with ^{12}C and ^{1}H are

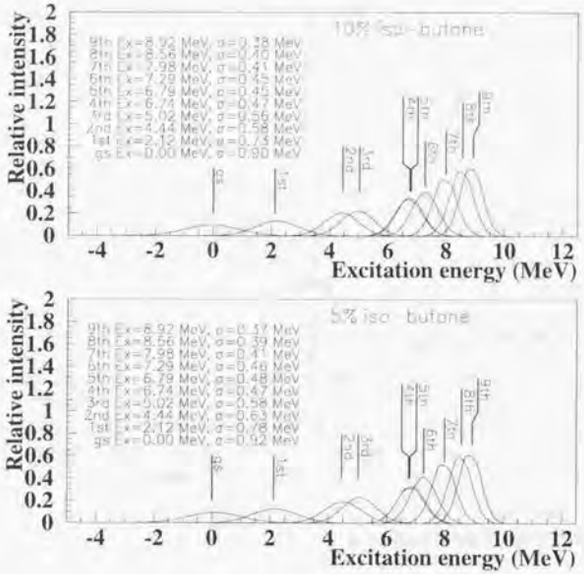

Figure 4.4: Simulated response functions for the various ^{11}B states. The upper figure is for the case of the 10%-isobutane-mixed gas and the lower figure is for the case of the 5%-isobutane-mixed gas. The horizontal axis shows the excitation energy of ^{11}B and the vertical axis shows the peak height. Only the results of fitting are shown, for better appearance.

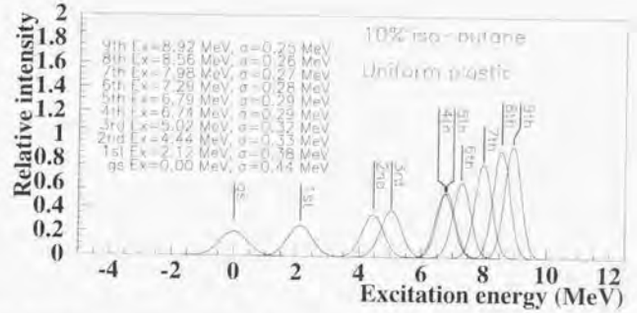

Figure 4.5: Excitation-energy spectrum of ^{11}B expected with the uniform F3 scintillator. The horizontal axis is the excitation energy (MeV) and the vertical axis is the relative intensity.

almost rejected, or essentially make no contribution. The details of analysis to select the true event and reject the background event are described in Chapter 5

4.4.2 Breakup reaction

Breakup reactions, ^{8}Li+^{4}He→^{7}Li+n+^{4}He, can occur. An example is shown in figure 3.15. Because they usually make a multiple-track event, they can be rejected easily. However if relative energy between the ^{4}He and the ^{7}Li is too small to produce a visible multiple track, it may be mixed in the true events. This may also occur for the case of ^{9}Be+^{4}He reaction.

^{8}Li+^{4}He reaction

The breakup channel, ^{8}Li+^{4}He→n+^{7}Li+^{4}He, opens above an energy of 2.03 MeV in the center-of-mass system, which corresponds to a ^{11}B excitation energy of 8.67 MeV.

Table 2.2 [37] gives the Γ_α and Γ_γ-decay widths of ^{11}B. Though the excited energy of the 9th excited state is above the threshold of the breakup, the breakup width (Γ_α) is negligibly small. Therefore, those excited states less than the 9th excited state are considered in the analysis. If events above the 9th excited state appear, they are all rejected by the analysis.

On the other hand, the direct breakup, ^{8}Li+^{4}He→(^{8}Li*+^{4}He)→n+^{7}Li+^{4}He, can contaminate the true events, if the relative energy between ^{7}Li and ^{4}He is small. In order to estimate the rejection efficiency against the breakup reaction, a simulation is performed. The breakup-reaction routine instead of the ^{8}Li(α,n)^{11}B reaction is programmed. It is assumed that the breakup occurs according to a one-step direct breakup, and that the angular distribution is isotropic in the rest-mass system of ^{8}Li*.

Figure 4.7 shows the overall efficiency of the ^{8}Li(α,n)α^{7}Li channels as a function of the excitation energy of ^{11}B. In order to compare this with the overall efficiency shown in figures 4.1 and 4.2, figure 4.7 shows the overall efficiency instead of the rejection efficiency. While the average of the overall efficiencies in figures 4.1 and 4.2 are typically 1%, the average of the overall efficiencies of breakup event is less than 0.3%, and is essentially negligibly small above

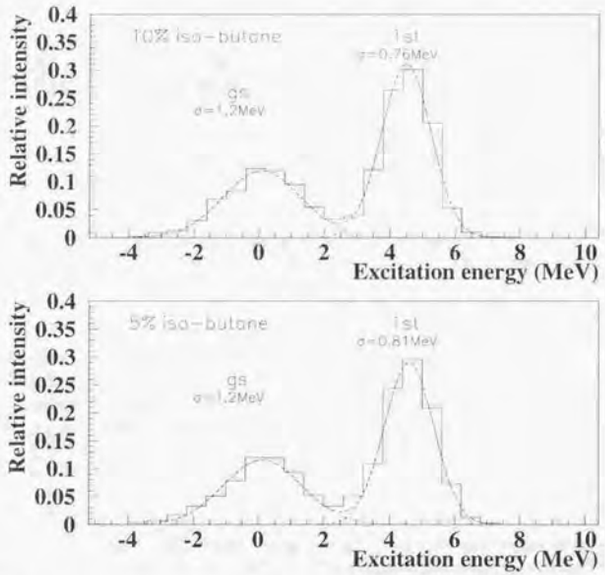

Figure 4.6: Response functions for the states of ^{12}C. The upper figure shows the 10%-isobutane-mixed-gas case, and the lower figure shows the 5%-isobutane-mixed-gas case. The horizontal axis is the excitation energy in MeV and the vertical axis is the relative intensity. The histograms are the results of a simulation-data analysis and the dotted lines are the results of fitting with the Gaussian.

9 MeV. Therefore, the present analysis can almost reject any multiple-track event.

If the breakup reactions have a much larger cross section than the ^{8}Li$(\alpha,n)^{11}$B reaction, they can make a broad peak above the threshold energy; however, their cross section is usually very small near to the threshold energy. Therefore, it seems that the background of the breakup reaction does not contribute to the spectrum shown in figure 5.10.

^{9}Be+^{4}He reaction

The breakup channel, ^{9}Be+^{4}He$\rightarrow n+^{8}$Be+^{4}He (or $n+3\alpha$), opens above an energy of 1.67 MeV (1.57 MeV for $n+3\alpha$) in the center-of-mass system, which corresponds to a ^{12}C excitation energy of 7.37 MeV (7.27 MeV for $n+3\alpha$). The 2nd excited state of ^{12}C is 7.654 MeV and decays to $\alpha+^{8}$Be with nearly 100% probability. Because the level property of ^{12}C is simpler than that of ^{11}B, the rejection of a breakup event is made simply by eliminating the event above a ^{12}C excitation energy of 7.27 MeV.

Other reactions

Even if other reactions with a smaller cross section occur, their effects can not appear in the present statistical level. They may become a problem for higher statistical measurement; however, they are not considered in the present analysis.

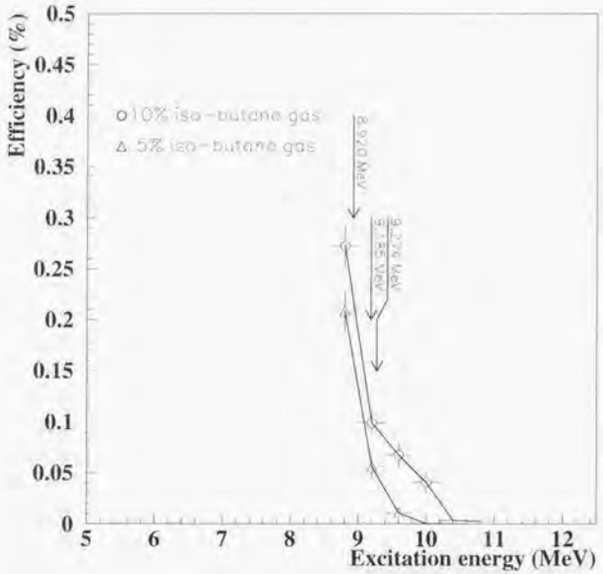

Figure 4.7: Overall efficiency for the breakup channel, ^{8}Li(α,n)α^{7}Li. The horizontal axis is the excitation energy (MeV) and the vertical axis is the overall efficiency (%). The circles show the 10%-isobutane-gas case, and the triangles show the 5%-isobutane-gas case. The 9th, 10th and 11th-excited states of ^{11}B are indicated. The efficiency is negligibly small above the 10th excited state, 9.185 MeV. Because the particle range in the 5%-isobutane-mixed gas is longer that in the 10%-isobutane-mixed gas, the former efficiency is lower than the latter efficiency.

Chapter 5

Analysis

5.1 Beam energy and intensity distribution

The beam energies were determined by the TOF between F2 and F3, and were corrected for energy losses in the F3-plastic scintillator and the entrance window of the MSTPC, as described in Subsection 2.2.3. The beam energies on each cathode pad were derived by calculating the energy loses passing through the detector gases. The energy-loss calculations were performed by Ziegler's code [45]. However, the result by the original code over-estimated the ranges to be slightly longer than the measured ranges in the gases; thus, the calculated stopping power (dE/dx) was increased by about a few % to reproduce the measured range.

The beam intensities were estimated by the total number of beams which satisfied the F2-F3 beam gates, the ratio of injection into the MSTPC measured by the SSD after the entrance window of the MSTPC, and the dead time of the DAQ system (about 50%). The beam-injection ratio is defined as

$$\text{beam-injection ratio} = \frac{\text{number of injected beam into the MSTPC}}{\text{number of beams passed the F2-F3 beam gate}} \cdot \qquad (5.1)$$

and its energy dependence is shown in figure 5.1. The beam energy was widely spreaded at the entrance of the MSTPC. Furthermore, it became to be more widely spreaded due to the energy loss while passing through the gases. Therefore, the distribution function of the effective-beam intensity which is took into account these factors is necessary for calculating the absolute cross section. Figure 5.2 shows the intensity distribution of the effective beam summed up over on all active cathode pads as a function of energy.

5.2 Event-selection procedure

In order to select only true events, the measured data are processed in 4 steps.

dE/dx of the first pad is used for selecting a beam with Z=3, and the first four ones are used to reject any undesirable beam events, like a scattered one by the entrance-window film or field-cage wires, or beam-pile-up events.

The first event gate is the dE/dx-range selection; the dE/dx of the 5th pad and the range plot is used to reject the beam without a reaction, elastic scattering at a forward angle and an event which emitted a light charged particle with a longer range. Figure 5.3 shows a plot of the dE-range gate. The dense locus is the beam event. The events within the solid line are accepted.

The second event gate is used to select out a single-track event by tracing the track. If the multiple track appears like in figure 3.15, it is rejected.

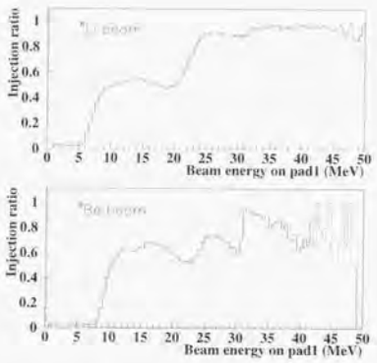

Figure 5.1: Energy dependence of the beam-injection ratio. The upper figure shows the dependence of ^{8}Li beams and the lower figure shows that of ^{9}Be beams. The horizontal axis is the beam energy on the first cathode pad and the vertical axis is the injection ratio. The spectrum structure may be due to the contributions of different charge states of the beam ions which match the magnetic rigidity of TQ3.

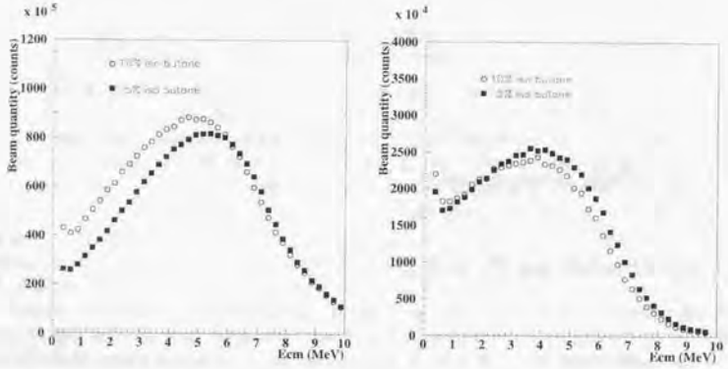

Figure 5.2: Beam-intensity distributions. The left-side figure shows the beam of ^{8}Li and the right-side figure shows that of ^{9}Be. The horizontal axis is the beam energy at the center-of-mass system in MeV and the vertical axis is the beam intensity in total count. The white circles show the distribution for the 10%-isobutane-mixed gas and the black squares show the distribution for the 5%-isobutane-mixed gas.

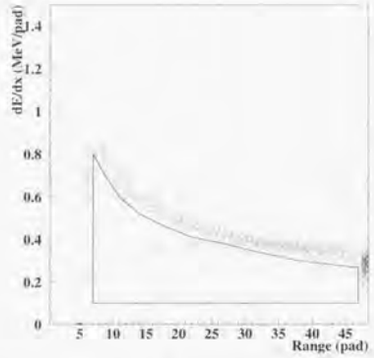

Figure 5.3: dE-range gate on the dE-range 2-dimensional histogram. The horizontal axis shows the measured range in unit of the pad number and the vertical axis shows the dE/dx on the 5th pad in MeV/pad. The plot is for the case of a ^{8}Li beam and the 10%-isobutane-mixed gas. The events inside the solid line are accepted.

The third event gate is used to detect any sudden change in dE/dx as in figure 3.13. If the amplitude of the dE/dx change is more than 0.2 MeV from the Bragg curve shown in figures 3.11 and 3.12, it is accepted. The dE/dx-change gap of 0.2 MeV is reasonable, since the dE/dx straggling is within 0.2 MeV. The reaction position and energy are determined by the pad where the dE/dx change is detected.

In these processes, the reaction energy and position are determined, and then the neutron TOF is also determined. The energy and momentum of ^{11}B can be derived from a kinematic calculation using the beam and neutron information.

The kinematic-calculation formula are

$$E_4 = E_1 + E_2 - E_3 \,, \tag{5.2}$$

$$\vec{P}_4 = \vec{P}_1 + \vec{P}_2 - \vec{P}_3 \,, \tag{5.3}$$

where E_i is the energy (kinetic-energy+mass) and $\vec{P}_i$ is the momentum. The subscripts have the following meanings: $i = 1$ is the beam (^{8}Li or ^{9}Be), $i = 2$ is the α target, $i = 3$ is the neutron and $i = 4$ is the product (^{11}B or ^{12}C).

The kinetic energy of $i = 4$ is described as

$$E_4^k = E_4 - M_4 \,, \tag{5.4}$$

$$M_4 = \sqrt{E_4^2 - \vec{P}_4^{\,2}} \,, \tag{5.5}$$

where E_i^k is the kinetic energy and M_i is the invariant mass.

The fourth event gate is used to trace the reaction products. The predicted track, range and dE/dx of ^{11}B, which are derived from a kinematic calculation, are compared with the measured ones. If they are consistent with each other within 30% accuracy, it is regarded as the true event. The kinematic effect by emitting a γ-ray from an excited ^{11}B* is very small, thus it is neglected. An accuracy of 30% is selected, since the analysis efficiency saturates (about 70$\sim$80%) with more than 30% accuracy. Figure 5.4 shows a typical event of the dE/dx spectrum. The upper figure shows the dE/dx spectrum of the real event which agrees with that of simulated one. The simulated spectrum is derived from the beam energy and momentum, and the neutron energy and momentum. The reactions with ^{12}C and ^{1}H are also simulated and are shown in the lower figure. They do not agree with the dE/dx spectrum of the real event at all. Therefore, this typical event is identified as the true ^{8}Li(α,n)^{11}B-reaction event. Another case of typical event is shown in figure 5.5.

Finally, the excitation function of the cross section and the excitation energy of the reaction products are derived. The excitation energy of the products, E_i^{ex}, is described as

$$E_4^{ex} = M_4 - M_4^0 \,, \tag{5.6}$$

where M_i^0 is the ground-state mass.

5.3 ^{8}Li(α,n)^{11}B reaction

Figure 5.6 shows the neutron TOF spectrum. The TOF is normalized at a constant flight path of 1.5 m in order to obtain an overview. A sharp γ-peak appears at 5 nsec, which agrees with the γ-ray TOF.

Figures 5.7 and 5.8 show the excitation-energy spectrum of ^{11}B analyzed by the procedure described above for the 10% and 5%-isobutane-mixed gas, respectively. In order to determine the individual branching ratio, the response function derived from simulations is used to fit the spectrum. The fitting parameters are only the heights of the Gaussian (A_i), while the centers (E_i) and standard deviations (σ_i) are fixed, because it is difficult to fit the present data with so many parameters. The centers are derived from the excitation energies, and the standard deviations are derived from the results of the simulations shown in figure 4.4.

The fitting function is

$$F(E) = \sum_{i=gs}^{9th} A_i \exp\left\{-\left(\frac{E-E_i}{\sqrt{2}\sigma_i}\right)^2\right\} , \tag{5.7}$$

under the condition $A_i \geq 0$. In order to reduce the number of fitting parameters, it is assumed that the 4th (6.74 MeV) and 5th (6.79 MeV) excited states have the same height, $A_4 = A_5$. The two states are very close and can not be distinguished due to the resolution of the present experiment.

The branching ratios are derived by calculating the area of the individual peak and taking the averaged overall efficiencies for each individual state. Of course, it is better to distinguish the individual states of ^{11}B and apply the overall efficiencies for them as a function of the reaction energies, event by event. However, it is difficult to distinguish them with the present resolution, so that the averaged overall efficiency, which is averaged by the energy, is applied. Table 5.1 gives the branching ratio obtained for the case of the 10%-isobutane-mixed gas and the 5%-isobutane-mixed gas. They are the average ratios for the energy region between 1.5 MeV and 7.0 MeV in the center-of-mass system.

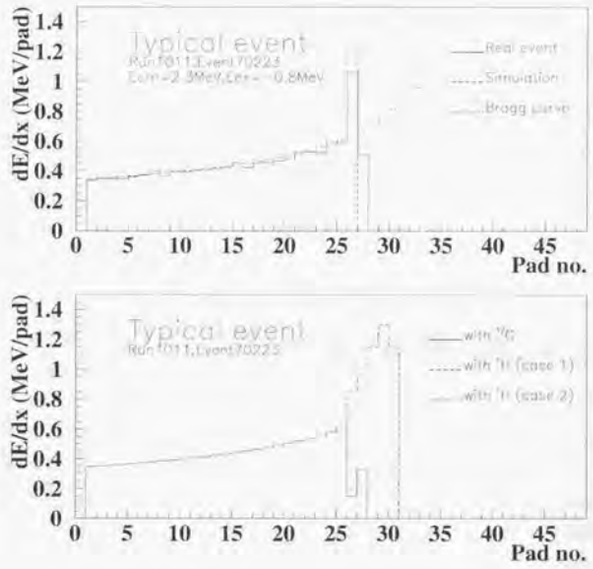

Figure 5.4: Typical event of the ^{8}Li(α,n)^{11}B reaction. The upper figure shows the dE/dx spectrum of the real event (solid line) and that of the simulated one (dashed line) calculated by the measured information. Since they agree very well with each other, this event is regarded as the true ^{8}Li(α,n)^{11}B-reaction event. The dotted line shows the Bragg curve of the ^{8}Li beam. This event occurred at the center-of-mass energy of 2.3 MeV, and the excitation energy of ^{11}B is -0.8 MeV, corresponding to the ground state of ^{11}B. The lower figure shows the simulations of the reaction with ^{12}C and ^{1}H. The solid line shows the case of the reaction with ^{12}C. The dashed line (case 1) shows the case of the reaction with ^{1}H, and two α particles are emitted at 0 and 180 degree in the rest-mass-system of them. The dotted line (case 2) shows the case of the reaction with ^{1}H, and two α particles are emitted at 90 degree in the rest-mass-system of them. Since the lower spectra do not agree with the upper one, the backgrounud events cannot be contaminated in the true event.

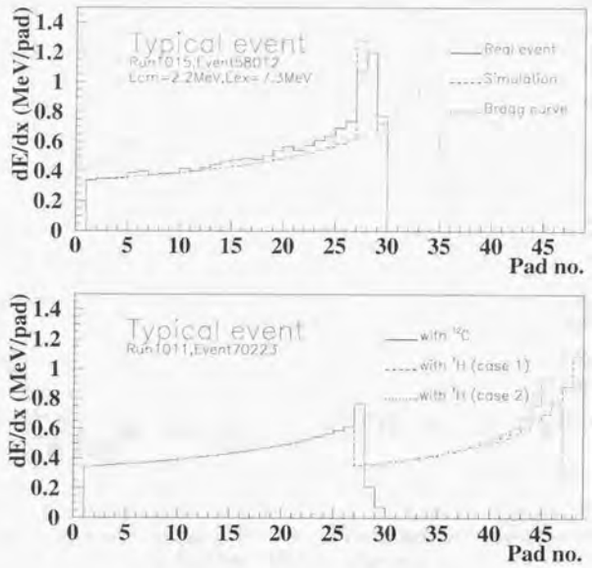

Figure 5.5: Another typical event of the ^{8}Li(α,n)^{11}B reaction. The notation of the lines are same as in figure 5.4. This reaction occurred at the center-of-mass energy of 2.2 MeV, and the excitation energy of ^{11}B is 7.3 MeV, corresponding to the 4th, 5th, 6th or 7th excited state.

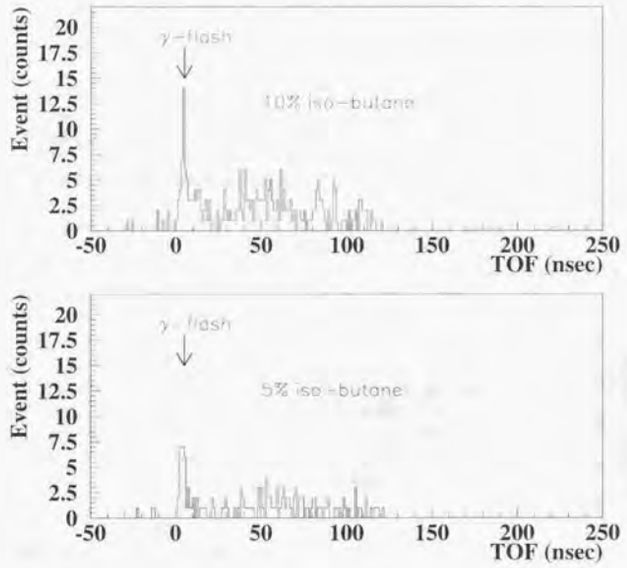

Figure 5.6: Neutron-TOF spectra for the ^{8}Li + any target reactions. The event which involves the sudden change of dE/dx is corrected. The horizontal axis is the TOF in nsec and the vertical axis is the total event number. The upper figure is the data for the 10%-isobutane-mixed gas, and the lower figure is the data for the 5%-isobutane-mixed gas.

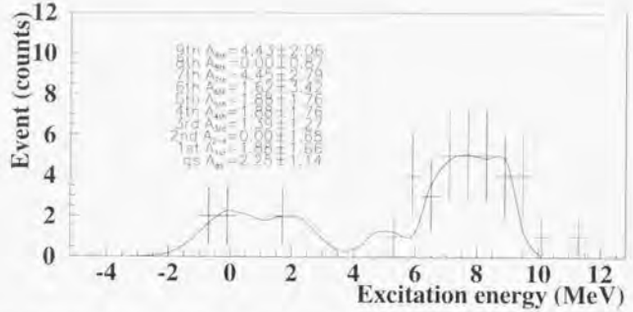

Figure 5.7: Excitation energies of ^{11}B measured with the 10%-isobutane-mixed gas. The horizontal axis shows the excitation energy in MeV and the vertical axis shows the number of events. The solid line is the result of a fitting and the crosses are the analyzed data. The error bar of the horizontal axis is the bin size and that of the vertical axis is only the statistical error.

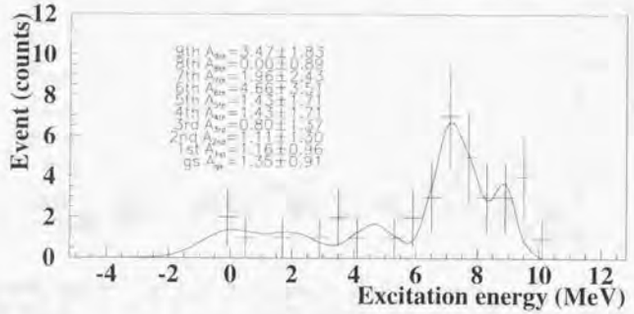

Figure 5.8: Excitation energies of ^{11}B measured with the 5%-isobutane-mixed gas. The horizontal axis shows the excitation energy in MeV and the vertical axis shows the number of events. The solid line is the result of a fitting and the crosses are the analyzed data. The error bar of the horizontal axis is the bin size and that of vertical axis is only the statistical error.

State	Ex (MeV)	Ratio(%) 10% iso-butane			5% iso-butane			Average		
9th	8.92	15.18	±	9.67	13.25	±	9.26	14.22	±	6.69
8th	8.56	0.0	±	2.75	0.0	±	3.23	0.0	±	2.12
7th	7.98	14.00	±	10.69	7.12	±	9.36	10.56	±	7.10
6th	7.29	5.68	±	12.22	19.21	±	16.78	12.45	±	10.38
5th	6.79	6.58	±	5.22	6.21	±	5.93	6.40	±	3.95
4th	6.74	6.82	±	5.42	6.40	±	6.10	6.61	±	4.08
3rd	5.02	7.31	±	7.41	4.94	±	8.77	6.13	±	5.74
2nd	4.44	0.0	±	9.84	8.33	±	10.44	4.17	±	7.17
1st	2.12	16.95	±	16.68	13.38	±	12.56	15.17	±	10.41
gs	0.00	27.48	±	18.42	21.15	±	17.05	24.32	±	12.55

Table 5.1: Averaged branching ratio. The left-hand two columns show the levels and their excitation energies. The branching ratio and its error are shown for the case of the 10%-isobutane-mixed gas, the 5%-isobutane-mixed gas and their average.

The efficiency to calculate the absolute total cross section is derived by averaging the overall efficiencies shown in figures 4.1 and 4.2 weighted by the branching ratio shown in table 5.1. Although it is also better to apply the overall efficiency for state by state and sum up the individual cross section, the present method is the most reasonable way to treat the present data. Figure 5.9 shows the averaged efficiencies for the case of the 10%-isobutane-mixed gas and the 5%-isobutane-mixed gas.

Figure 5.10 shows the excitation function of the total cross section corrected for the efficiency of figure 5.9. The total event number is small and the peak resolution is not sufficiently good to distinguish any individual state; therefore, the individual excitation functions of the cross section can not be determined. They include all of the states from the ground state to the 9th excited state. By comparing the 10% and 5%-isobutane-mixed-gas data, it seems that the effect of background events caused by the mixed ^{12}C or ^{1}H is not significant.

5.4 ^{9}Be(α,n)^{12}C reaction

In order to examine the performance of the present experimental setup, the ^{9}Be(α,n)^{12}C reaction, whose cross sections and angular distributions were already well measured and are available in the region of center-of-mass energies from 0.2 to 5.2 MeV [24, 25, 26, 27, 28], was also measured with the same system after the ^{8}Li(α,n)^{11}B-reaction measurement. The measurement and analysis were performed by the same procedure and same method as those of the ^{8}Li(α,n)^{11}B reaction.

Figure 5.11 shows the TOF spectrum of the neutron detectors. The flight length is normalized at 1.5 m where the γ-flash peak appears at 5 nsec.

Figure 5.12 shows the excitation-energy spectrum of ^{12}C. They are integrated events over center-of-mass energies between 2.0 and 5.2 MeV. Three peaks appear and each state can be assigned to well-known levels of ^{12}C. The same fitting procedure as for the ^{8}Li(α,n)^{11}B reaction are performed for the ground state and the 1st excited state. The states above the 2nd

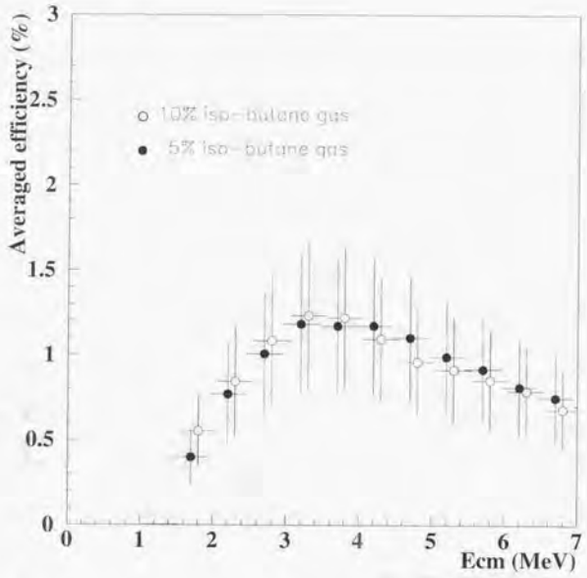

Figure 5.9: Averaged efficiency of the excitation function for the ^{8}Li(α,n)^{11}B reaction. The horizontal axis is the center-of-mass energy (MeV) and the vertical axis is the efficiency (%) including all factors. The white circles indicate the efficiency for the case of the 10%-isobutane-mixed gas, and the black circles indicate that for the case of the 5%-isobutane-mixed gas. For a better look, the horizontal-axis points of the white circles are shifted by +0.05 MeV, and those of the black circles are shifted by −0.05 MeV.

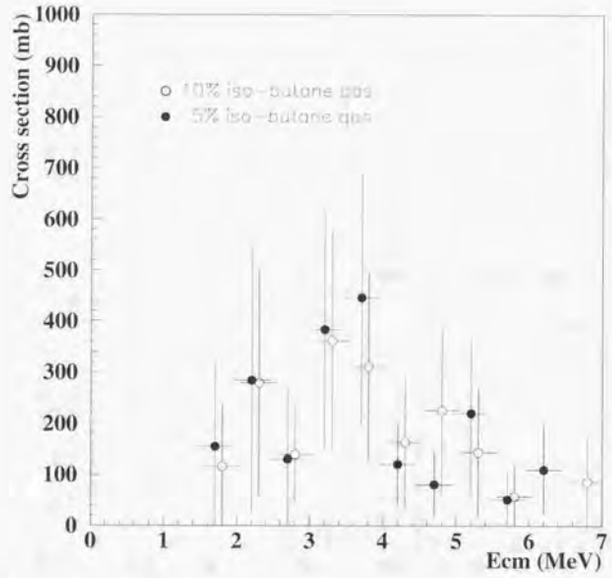

Figure 5.10: Excitation function of the total cross section for the ^{8}Li(α,n)^{11}B reaction. The horizontal axis is the center-of-mass energy (MeV) and the vertical axis is the absolute cross section (mb). The white circles indicate the data for the 10%-isobutane-mixed gas, and the black circles indicate that for the 5%-isobutane-mixed gas. For a better look, the horizontal-axis points of the white circles are shifted by +0.05 MeV, and those of the black circles are shifted by −0.05 MeV.

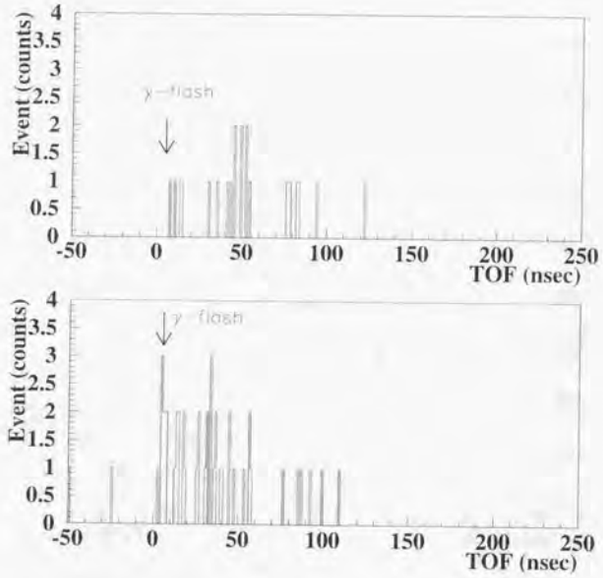

Figure 5.11: Neutron-TOF spectra for the ^{9}Be + any target reaction. The horizontal axis is the TOF in nsec and the vertical axis is the number of events. The upper figure shows the TOF spectrum for the case of the 10%-isobutane gas , and the lower figure shows that for the case of the 5%-isobutane gas. The γ-flash peak appears at 5 nsec.

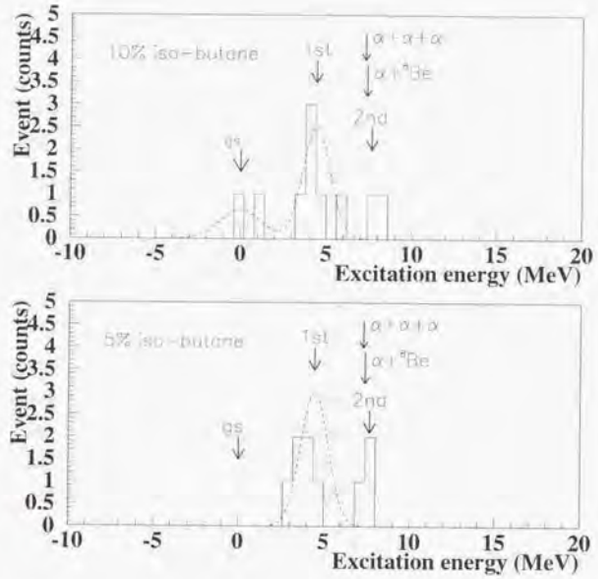

Figure 5.12: Excitation-energy spectrum of ^{12}C. The horizontal axis means the excitations energy in MeV and the vertical axis means the number of events. The upper figure shows the case of the 10%-isobutane-mixed gas, and the lower figure shows the case of the 5%-isobutane-mixed gas. The dotted line shows the response function estimated by simulations. Each peak can be assigned to the ground state (0 MeV), the 1st excited state (4.44 MeV) and the 2nd excited state (7.65 MeV).

excited states can be neglected, because all of them lead to breakup channels, as described in Subsection 4.4.2.

In the case of ^{12}C, the ground state and 1st excited state are sufficiently separated, even at the present resolution, as opposed to the ^{11}B. The event-selection windows for an individual state of ^{12}C can be set and the individual cross sections can be determined.

Figure 5.13 shows the individual cross sections measured with the 10%-isobutane-mixed gas. Figure 5.14 shows the total cross section, which is the sum of the ground-state and 1st-excited-state cross sections. They are derived in the same way as for the ^{8}Li(α,n)^{11}B-reaction cross section. The efficiencies were estimated by the simulations shown in figure 4.3. The overall efficiencies with the angular distribution of the reference data were used for the present analysis. The ground-state cross section, the 1st-excited-state cross section and the total cross section are shown as 1 MeV bin-size and 3 MeV bin-size. In spite of the low statistics and large error bars, the measured cross sections agree well with the reference cross sections.

Figure 5.15 shows the cross sections to the 1st excited state measured with the 5%-isobutane-mixed gas. In this case, the ground-state event was not observed due to low statistics, so that only the 1st-excited-state cross sections were determined. The agreement with the reference cross sections is also good. Both the 10%-isobutane-mixed-gas data and the 5%-isobutane-mixed-gas date are consistent with the reference data, and the 10%-isobutane-mixed-gas data and 5%-isobutane-mixed-gas data are consistent with each other within the error bars; also the effect of background events, e.g. reactions with ^{12}C or ^{1}H, are not discernible.

According to this study, it was confirmed that the present experimental setup and simulation procedure are effective and reliable to measure ^{8}Li(α,n)^{11}B-type reactions.

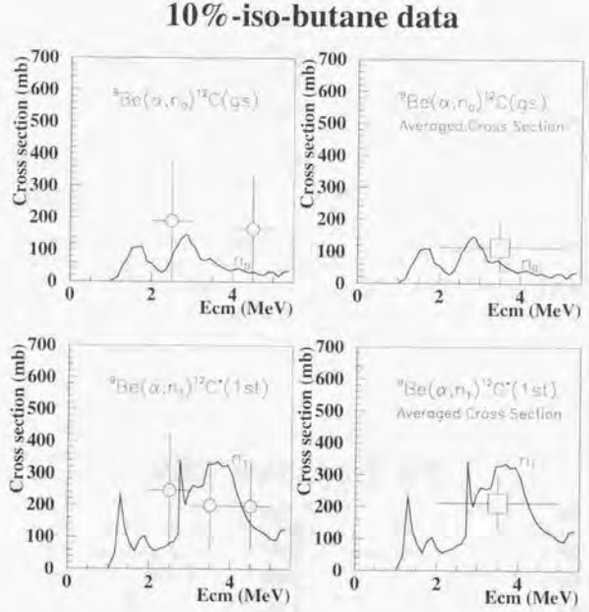

Figure 5.13: Individual cross sections of the ^{9}Be(α,n)^{12}C reaction measured with the 10%-isobutane-mixed gas. The upper figure shows the ground-state cross sections and the lower figure shows the 1st-excited-state cross sections. The left-side figure was calculated with a 1 MeV bin-size and the right-side figure was calculated with a 3 MeV bin-size. The solid lines show the cross sections from references [24, 25, 26, 27, 28]. n_0 means the cross section to the ground state and n_1 means the cross section to the 1st excited state.

10%-iso-butane data

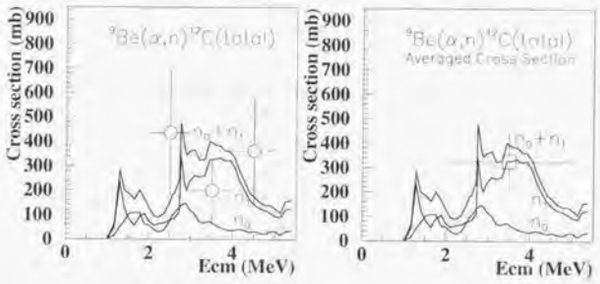

Figure 5.14: Total cross sections of the ^{9}Be(α,n)^{12}C reaction measured with the 10%-isobutane-mixed gas. The left-side figure was calculated with a 1 MeV bin-size and the right-side figure was calculated with a 3 MeV bin-size. The solid lines mean the cross sections from references [24, 25, 26, 27, 28]. n_0 means the cross section to the ground state and n_1 means the cross section to the 1st excited state.

5%-iso-butane data

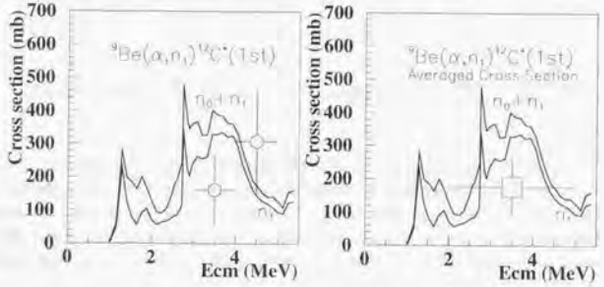

Figure 5.15: 1st-excited-state cross section of the ^{9}Be(α,n)^{12}C reaction measured with the 5%-isobutane-mixed gas. The left-side figure was calculated with a 1 MeV bin-size and the right-side figure was calculated with a 3 MeV bin-size. The solid lines mean the cross sections from references [24, 25, 26, 27, 28]. n_0 means the cross section to the ground state and n_1 means the cross section to the 1st excited state.

Chapter 6

Results and Discussion

6.1 Present results

6.1.1 Comparison with previous experiments

Figure 6.1 shows the present result of the averaged cross section of the 10%-isobutane-gas data and the 5%-isobutane-gas data together with other data for a comparison. The other data indicate the cross section of the ^{8}Li(α,n$_0$)^{11}B(gs) measured by an inverse reaction [12], that of the *direct-inclusive measurements* by using the MUSIC at RIKEN [14] and at the Notre Dame-Michigan-Ohio State radioactive-beam facility [15].

The present data for the *direct-exclusive measurement* show a lower cross section than that of the *direct-inclusive measurements* over the entire energy region. In order to compare them easily, the averaged cross sections between the energy region of 1.5 MeV and 5.0 MeV are given in table 6.1. The ground-state cross section of the present data agrees with that of the inverse-reaction measurement within the statistical error.

The reason that two direct measurements disagree may be due to systematic errors relevant to previous measurements. Figure 6.2 shows a typical event which cannot be distinguished from a background event in an inclusive measurement. In this case, the elastic-scattering event gives a very similar dE/dx pattern to the true event. There are many reaction candidates which give confusing event patterns, and it is difficult to reject them by the inclusive measurement. According to the papers of previous experiments [14, 15], they estimated the effect of the elastic scattering by computer simulation and subtracted the background events. It seems that the

	Cross section (mb)	
	Total	Ground state
Present	228.3±47.1	55.52±30.85
Inclusive	418.3±26.7	N/A*
Inverse	N/A*	74.07±0.33

Table 6.1: Averaged cross sections between 1.5 MeV and 5.0 MeV. The top row is the present data, the center row is the *direct-inclusive measurement* data, and the bottom row is data derived from the inverse-reaction measurement. The center column is the total cross section and the right column is the ground-state cross section. The ground-state cross section of the present data was calculated using the branching ratio given in table 5.1. (*Not Available.)

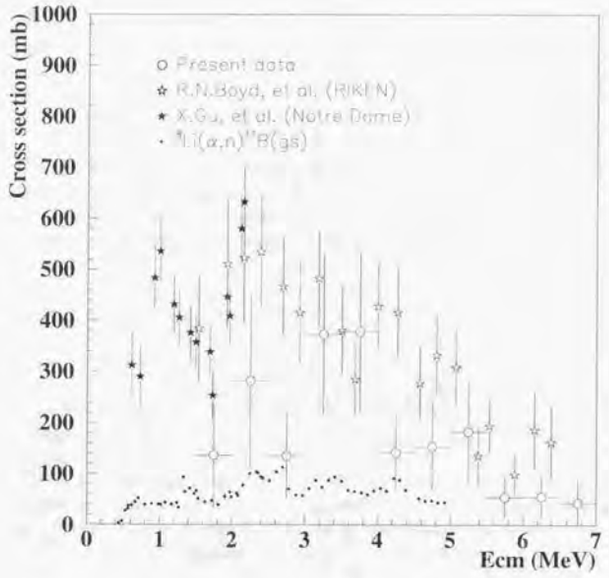

Figure 6.1: Excitation function of the cross section for the ^{8}Li(α,n)^{11}B reaction. The horizontal axis is the center-of-mass energy (MeV) and the vertical axis is the absolute cross section (mb). The white circles indicate the present data. The black dots indicate the ground-state cross section. The white stars and black stars indicate the data of the *direct-inclusive measurements*.

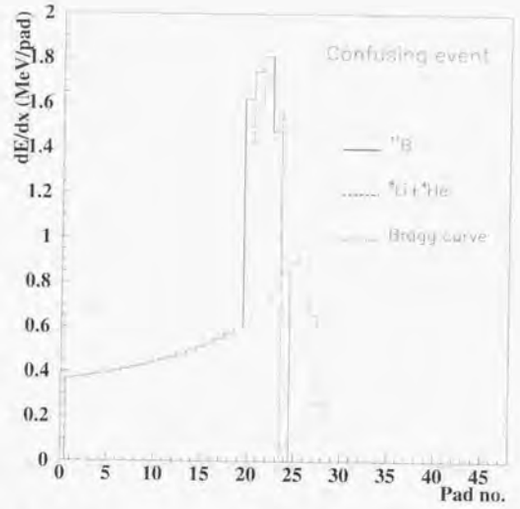

Figure 6.2: Typical confusing event in the inclusive measurement. The dE/dx-pattern spectrum is shown. The solid line shows the dE/dx pattern of the ^{8}Li(α,n$_0$)^{11}B(gs) reaction with emitting a neutron at the direction of 30 degree in the center-of-mass system. The dashed line shows the dE/dx pattern of the elastic-scattering, ^{8}Li(α,α)^{8}Li reaction in the case of head-on collision. The former can not be distinguished from the latter in the inclusive measurement. The dotted line shows the Bragg curve of ^{8}Li.

estimation would not be precise enough and the subtraction would not be sufficient.

We believe that we made any systematic errors in our measurements as small as possible by utilizing a better performance of the MSTPC together with the use of neutron counters, which should have produced a sufficiently high achievement of event selection. It should also be noted that the present data agree with the ground-state cross section measured by the inverse reaction within the statistical error, although the error is not small.

6.1.2 Comparison with the theoretical calculations

On the other hand, theoretical calculations were performed by T. Rauscher et al. [46] and P. Descouvemont [47]. T. Rauscher et al. tried to reproduce the cross section of the ^{8}Li(α,n$_0$)^{11}B(gs) reaction and produce the total cross section of the ^{8}Li(α,n)^{11}B reaction. Their work had been done before the *direct-inclusive measurement* was performed, and gave the total cross section which was larger than the ground-state cross section by a factor of about 1.3. P. Descouvemont tried to reproduce the both of the ground-state cross section and the total cross section. Ac-

cording to his work, if the total cross section was reproduced, the ground-state cross section was overestimated by a factor of about 1.5. It seems that the theoretical results provide the smaller ratio between the ground-state cross section and the total cross section, thus favor the present result.

In the following sections, discussions about primordial nucleosynthesis with the present data are presented.

6.2 Nucleosynthesis in the early universe

6.2.1 Rate equation

Nucleosynthesis proceeded from $t = 0.01$ to 100 sec (corresponding to $T = 10$ MeV to 0.1 MeV) after the Big Bang, while the universe was expanding and cooling. The time development of the number density of an element is described as

$$\frac{d}{dt}n_i = \sum_{jkl}[< \sigma v >_{k,l\to i,j} n_k n_l - < \sigma v >_{i,j\to k,l} n_i n_j] + (\text{three body and other reaction}) - \frac{1}{\tau_i}n_i + (\text{other weak reaction}) + \nabla D_i \nabla n_i \ , \tag{6.1}$$

where n_i is the number density of element i, $< \sigma v >$ is the reaction rate given by the cross section (σ) and the relative velocity (v), depending on the temperature. The first term is a producing process of element i by a two-body reaction, $k + l \to i + j$; the second term is a reducing process of element i by a two-body reaction, $i + j \to k + l$; and the third term is other strong reactions. The fourth term is a decaying process by β-decay with a lifetime of τ_i, and the fifth term is other weak reactions. The sixth term is a diffusing-out process.

The present experiment gives a new reaction rate, which is one of the reducing processes of $i = {}^8$Li, as well as one of the producing process of $i = {}^{11}$B. In order to estimate the effect quantitatively based on the present cross-section data of the ^{8}Li(α,n)^{11}B reaction, the method used to derive the reaction rate was described in the following subsections.

6.2.2 Reaction rate and astrophysical S factor

The averaged reaction rate of the $i+j \to k+l$ reaction with temperature T is given by averaging the excitation function of the cross section, $\sigma(E)$, with the Maxwell-Boltzmann distribution,

$$< \sigma v >= \sqrt{\frac{8}{\pi A}}(kT)^{-3/2}\int_0^\infty \sigma(E) E \exp(-\frac{E}{kT})dE \ , \tag{6.2}$$

where E is the center-of-mass energy, k is the Boltzmann constant, and A is the reduced mass, $A = \frac{A_i A_j}{A_i + A_j}$.

Here, it is useful to introduce the astrophysical S factor, which is derived from the cross section by taking out the $1/v$ effect and the penetrability factor of the Coulomb barrier for a reaction between charged particles. The formalism of the astrophysical S factor, $S(E)$, is described in Appendix B.1. By substituting equation B.4 into equation 6.2, the averaged reaction rate is expressed as

$$< \sigma v >= \sqrt{\frac{8}{\pi A}}(kT)^{-3/2}\int_0^\infty S(E)\exp(-\sqrt{\frac{E_g}{E}} - \frac{E}{kT})dE \ , \tag{6.3}$$

and can therefore be calculated if $S(E)$ is given.

We tried to construct $S(E)$ based on the present data. The most-important energy region for the ^{8}Li(α,n)^{11}B reaction is around an energy of 0.6 MeV, where the Gamov peak $T_9 = 1$ is located. However, the cross-section data below 1.5 MeV at the center-of-mass energy was not obtained by the present measurement, so that extrapolations using the ground-state cross section, which was derived from the inverse reaction, should be performed. Here, we assume three cases; the first one is that the ground-state cross section is multiplied by a factor of 2.6, which is determined by comparing the total cross section measured by the present experiment and the ground-state cross section measured by the inverse reaction between center-of-mass energies of 1.5 MeV and 2.0 MeV. The second one is that the ground-state cross section is multiplied by a factor of 3.1, which is determined by comparing the total cross section measured by the present experiment and the ground-state cross section measured by the inverse reaction between center-of-mass energies of 1.5 MeV and 5.0 MeV. The third one is that the ground-state cross section is multiplied by a factor of 4.1, which is the ratio of the total cross section to the ground state one in the present result, averaged between 1.5 MeV to 5.0 MeV.

However, it seems that a factor of 2.6 is better than that of 3.1 and 4.1, since the channel to the higher excited states of ^{11}B, which can not be populated from the lower energy region below 2.0 MeV, may be included for factors of 3.1 and 4.1. For comparing them, the both extremes cases, factors of 2.6 and 4.1, are illustrated in figure 6.3. On the other hand, R. N. Boyd [14] and X. Gu [15] suggest a factor of 5. This factor is larger than any present case.

For a numerical calculation, any physical constants were explicitly substituted in equation 6.3 as

$$< \sigma v >= 6.1968 \times 10^{-14} A^{-1/2} T_9^{-3/2} \int_0^\infty S(E)\exp(-\sqrt{E_G/E} - 11.605E/T_9)dE \quad [\mathrm{cm}^3/\mathrm{sec}], \tag{6.4}$$

where T_9 is in unit of $T = 10^9$ K and $S(E)$ is in unit of MeV-barn.

6.2.3 Reaction rate of the ^{8}Li(α,n)^{11}B reaction

Though the value of $< \sigma v >$ can be obtained by carrying out a numerical integration of equation 6.4 for various T_9, an analytic formula of equation 6.2 as a function of T_9 is convenient for a nucleosynthesis calculation. The details concerning the formalism of the reaction rate are described in Appendix B.2. We first obtained the value of $< \sigma v >$ for several T_9 points, and then fit it by the analytical formula.

Figure 6.4 shows the present result of the ^{8}Li(α,n)^{11}B-reaction rate as a function of the temperature around $T_9 = 1$. The solid line shows the result of fitting the numerical result with a factor of 2.6 and the dashed line shows that with a factor of 4.1. The result given by X. Gu et al. [15] is also plotted by the dotted line.

The obtained function for a factor of 2.6 is

$$N_a < \sigma v > = T_9^{-3/2}[2.66 \times 10^5 \exp(-4.41/T_9) + 3.00 \times 10^8 \exp(-6.73/T_9)] + 1.02 \times 10^{13}\exp(-19.46/T_9^{1/3}) + 8.82 \times 10^9 \exp(-19.47/T_9) \quad [\mathrm{cm}^3/\mathrm{sec/mole}], \tag{6.5}$$

and that for a factor of 4.1 is

$$N_a < \sigma v > = T_9^{-3/2}[1.30 \times 10^6 \exp(-4.41/T_9) + 5.24 \times 10^8 \exp(-6.73/T_9)] + 1.07 \times 10^{13}\exp(-19.46/T_9^{1/3}) + 1.23 \times 10^{10} \exp(-19.47/T_9) \quad [\mathrm{cm}^3/\mathrm{sec/mole}], \tag{6.6}$$

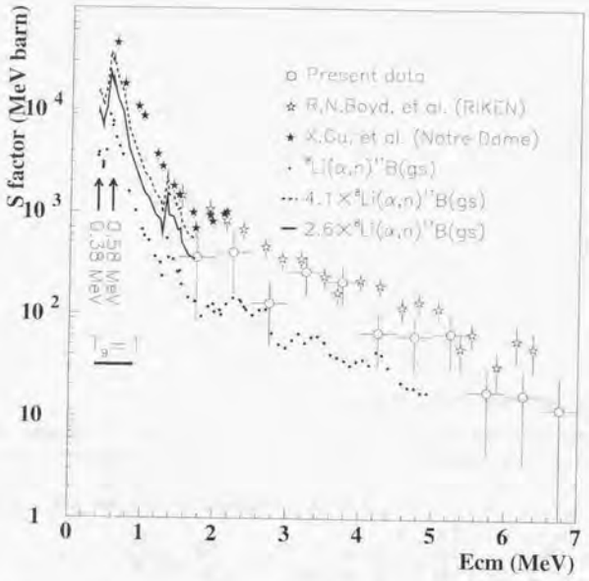

Figure 6.3: Astrophysical S factor. The horizontal axis is the center-of-mass energy (MeV) and the vertical axis is the astrophysical S factor (MeV·barn). The white circles are the present data, the white and black stars are the *direct-inclusive-measurement* data, and the black dots are the ground-state data. The extrapolated data multiplied the ground-state data by a factor of 2.6 and 4.1 below 1.5 MeV are shown by a solid line and a dotted line, respectively.

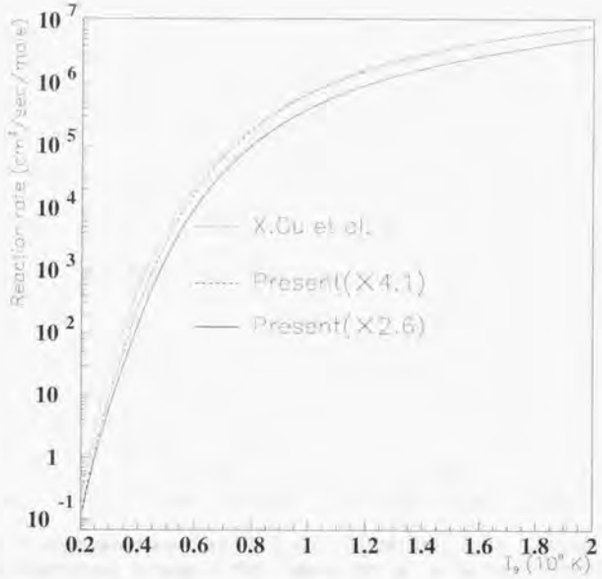

Figure 6.4: Reaction rate of the ^{8}Li(α,n)^{11}B reaction as a function of temperature. The horizontal axis is the temperature T_9 (10^9 K), and the vertical axis is the reaction rate in units of cm^3/sec/mole. The solid line is a plot of equation 6.5 and the dashed line is a plot of equation 6.6. The dotted line shows the function indicated by X. Gu et al. [15].

where N_a is Avogadro's number.

Because it is claimed that the ^{8}Li(α,n)^{11}B reaction occurs around $T_9 = 1$, according to equation B.14 and B.17, the effective energy and width are $E_0 = 0.62$ MeV and $\delta E_0 = 0.53$ MeV, respectively. The first and second terms of equations 6.5 and 6.6 are the resonance components for $E_r = 0.38$ MeV and 0.58 MeV, which are within the effective-energy width. The other resonances were not considered, since their energies were much higher than the effective energy region. The third term is the unsaturated continuum and the fourth term is the saturated continuum. The detailed meanings of these terms are described in Appendix B.2.

The reaction rate of the present data with a factor of 2.6 is about half of the reaction rate of the present data with a factor of 4.1. The present result for a factor of 4.1 is slightly less than the result of X. Gu et al.. Because the cross sections around the Gamov peak are most effective for the reaction rate, the reaction rate strongly depends on the factor.

	Present($\times$2.6)	Present($\times$4.1)	X. Gu et al.	Excluded ^{8}Li(α,n)^{11}B
SM ($\Omega_B h_{50}^2 = 0.04$)		7.37×10^{-15}		
IM ($\Omega_B h_{50}^2 = 0.2$)	3.58×10^{-13}	4.27×10^{-13}	4.50×10^{-13}	2.65×10^{-13}
(ratio)	(1.35)	(1.61)	(1.70)	(1.00)
IM ($\Omega_B h_{50}^2 = 1.0$)	1.21×10^{-9}	1.66×10^{-9}	1.82×10^{-9}	4.06×10^{-10}
(ratio)	(2.98)	(4.09)	(4.48)	(1.00)

Table 6.2: Summary of the mass fraction of ^{12}C. The ratio normalized by the factor without the ^{8}Li(α,n)^{11}B reaction is also indicated.

6.2.4 Primordial nucleosynthesis

In order to estimate the effect quantitatively in primordial nucleosynthesis by the reaction rate of the ^{8}Li(α,n)^{11}B reaction, theoretical calculations were performed by Y. Yamamoto [18].

The results of the calculation are presented as the mass fraction, X_A, which is defined as

$$X_A = \frac{An_A}{\sum_{A=\alpha,p,d,\ldots} An_A}\ , \tag{6.7}$$

where X_A is normalized as $\sum X_A = 1$.

Figure 6.5 shows the result of the mass fractions in the SM, which is assumed to be the uniform baryon density with $\Omega_B h_{50}^2 = 0.04$, which accounts for the observed abundances of ^{1}H, ^{4}He, and ^{7}Li. Here, h_{50} is related to the Hubble constant (H), where $H = 50 \times h_{50}$ km/Mpc/sec and $0.8 < h_{50} < 2$.

Figures 6.6 and 6.7 show the mass fractions in the IM, which is assumed to be the inhomogeneous baryon density with $\Omega_B h_{50}^2 = 0.2$ and $\Omega_B h_{50}^2 = 1.0$, respectively. The case of $\Omega_B h_{50}^2 = 0.2$ accounts for the observed abundances of ^{1}H, ^{4}He, and ^{7}Li, and the case of $\Omega_B h_{50}^2 = 1.0$ assumes that all masses of the universe consist of baryonic matter. A summary of the mass fraction of ^{12}C predicted by these calculations is given in table 6.2.

Although the abundances of ^{12}C calculated by the present reaction rate is reduced less than that by the reaction rate given by X. Gu et al, the abundances are still enhanced by a factor of $30 \sim 60\%$ for the case of $\Omega_B h_{50}^2 = 0.2$ and $200 \sim 300\%$ for the case of $\Omega_B h_{50}^2 = 1.0$, as compared with the case without the ^{8}Li(α,n)^{11}B reaction. The higher is the baryon density, the larger is the factor, so that the ^{8}Li(α,n)^{11}B reaction is more important in the universe with a higher baryon density. It is also noted that the abundance of ^{12}C in any case of the IM universe is much larger than that in the SM universe.

6.3 Summary and conclusion

The total cross section and branching ratio of the ^{8}Li(α,n)^{11}B reaction, which were not obtained simultaneously by previous experiments, were determined. Although the important energy region around the Gamov peak, $E_0 = 0.6$ MeV, could not be measured due to the limited statistics and resolution, it has been proved that the present detector system and analysis process provide a powerful method for measuring the ^{8}Li(α,n)^{11}B reaction.

The present measurement suggests that the total cross section to the ground state one is a factor of 2.6, which is lower than that of the *direct-inclusive measurements*, a factor of 5. However, the effect for primordial nucleosynthesis is still large compared to the case of no ^{8}Li(α,n)^{11}B

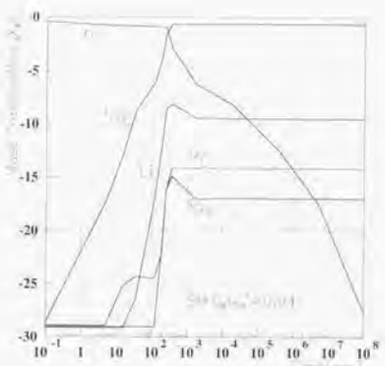

Figure 6.5: Abundances of the SM calculation for $\Omega_B h_{50}^2 = 0.04$.

reaction, especially for a high-baryon-density IM universe. Although it seems to be difficult to observe the abundances of elements heavier than A = 12 in primordial nucleosynthesis, because stellar nucleosynthesis is equal to or more than the primordial one, and they might not be distinguishable. When a much more precise observation of, for example, old-metal-poor stars can be able to be performed, a signal of the inhomogeneous Big Bang might be found.

On the other hand, almost all of the nuclear reactions in nucleosynthesis, which involve the unstable nuclides, have not yet been measured. Theoretical calculations can be improved by measuring such cross sections. It has also been proved by the present experiment that the present detector system and analysis process are very powerful for measuring the I(α,n)J-type reactions with the limited-intensity of RI beams. Furthermore, not only the I(α,n)J-type reaction, but also the I(p,n)J and I(d,n)J-type reactions, can be measured with the present system by utilizing p or d-rich gas. By cooperating with other trigger counters, the I(α,p)J and I(p,α)J-type reactions can also be measured. In addition, recent developments concerning the RI-ion source have made it possible to provide mono-energy and low-energy beams with reasonable intensity. As shown in figure 4.5, the measurement quality can be improved by using a mono-energy beam, due to the good energy resolution. The cross sections at lower energy regions, where it is difficult to achieve by the projectile-fragment-separation method, can also be measured.

We are sure that the present method will enable us to provide a breakthrough for new regions of the RI-beam experiment, especially in astrophysical nuclear physics.

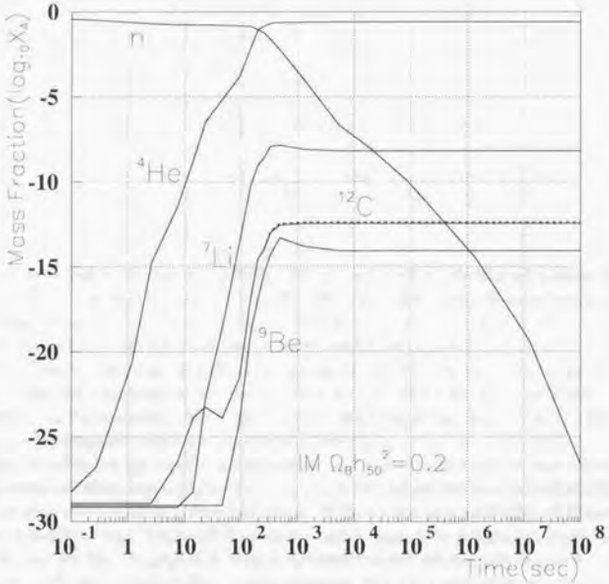

Figure 6.6: Abundances of the IM calculation for $\Omega_B h_{50}^2 = 0.2$. A factor of 2.6 was applied. For comparing the abundance of ^{12}C, the result of the calculation for a factor of 4.1 is also indicated by the dashed line.

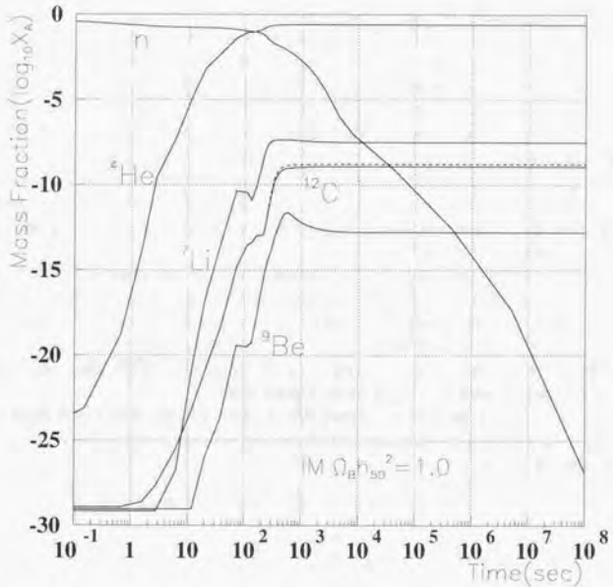

Figure 6.7: Abundances of the IM calculation for $\Omega_B h_{50}^2 = 1.0$. A factor of 2.6 was applied. For comparing the abundance of ^{12}C, the result of a calculation for a factor of 4.1 is also indicated by the dashed line.

Acknowledgment

I would like to express my best regards to my supervisor, Prof. T. Fukuda, who suggested me this interesting subject. He also gave me continuous encouragement and valuable advice. I express my sincere gratitude to Prof. M. Ishihara, who supported our experiment at RIKEN.

I would like to express my great appreciation to Mr. Y. Matsuyama, who supported and advised me concerning the construction of the MSTPC. Without his support and advice, we could not have completed its construction. I would also like to express my appreciation to Mr. M. Hirai, who constructed the New MUSIC which was the prototype of the MSTPC, and gave much advice concering the design of the MSTPC. I acknowledge Mr. H. Kobinata, who tested and improved the UNIDAQ and the flash ADCs. I also acknowledge Mr. J. Nakano and Mr. T. Miyachi. The MSTPC was constructed by their powerful collaboration. I would like to acknowledge Prof. K. Kimura and Mr. H. Kumagai, who presented thequnical advice and idea concerning the design of the MSTPC.

I am indebted to the collaborators of the experiment at RIKEN. I thank Mr. Y. X. Watanabe, Dr. A. Yoshida, Dr. Y. Watanabe, Dr. H. Sakurai, Dr. N. Aoi, Mr. M. Notani, Mr. N. Fukuda and Mr. K. Yoneda. Sincere gratitude is extended to the staff members of RARF for their operation.

I would like to thank Mr. M. Sasaki and Prof. H. Miyatake. They allowed us to use their neutron counters and simulation program, with good grace.

I would also like to express great appreciation to Dr. Y. Yamamoto and Prof. T. Kajino. They performed calculations of the primordial nucleosynthesis and gave me much theoretical advice about the IM universe.

Appendix A

Efficiency of the neutron counter

The efficiencies of the neutron counters were measured using neutrons from the fission source of ^{252}Cf after an experiment with the same setup. The ^{252}Cf was firmly fastened at the center of the neutron-barrel radius and was stuck fast to a small (100 μm thick and 50 mm^2)-size-surface-barrier-type SSD. For distinguishing from α particles, the fission fragments were detected by the SSD. The SSD was also used as a trigger signal of the DAQ and a start signal to measure the neutron TOF.

The neutron distribution from the fission source can be described by the Maxwellian [49]

$$f(E) = \frac{2E^{1/2}}{\pi^{1/2}T^{3/2}} \exp\left(-\frac{E}{T}\right) , \tag{A.1}$$

where $\int_0^\infty f(E)dE$ is normalized to be 1, E is the energy of the neutron and T is a nuclear temperature, T = 1.42 MeV, for the ^{252}Cf.

By a recent study [50], the averaged number of neutrons per fission, $\bar{\nu}$, is 3.65±0.23. Therefore, the energy and number distribution of the fission neutron is

$$N_0(E) = \bar{\nu} f(E) . \tag{A.2}$$

The efficiency of the neutron counters is determined to be

$$\varepsilon(E) = \frac{4\pi N(E)}{\Delta\Omega N_0(E)} , \tag{A.3}$$

where $N(E)$ is the number of detected neutrons and $\Delta\Omega$ is the solid angle covered by the neutron counter.

Figure A.1 shows the TOF spectra. The γ-flash peak is at 5 nsec, because the flight-path length was 1.5 m. The time resolution derived by the γ-flash peak is about 3 nsec (FWHM). A throughing correction was not made, because it was not effective for the present experiment.

Figure A.2 shows the efficiencies of the neutron counters. Although the thresholds of the neutron counters were set at around 10 $\sim$ 20 keVee by using the Compton edge of the γ ray of ^{137}Cs and ^{133}Ba, the thresholds were determined by a computer simulation [33] in order to represent the efficiencies measured with the fission source, which resulted in around 15 $\sim$ 25 keVee. Because the neutron-energy spectrum is a continuum, the threshold determined by the simulation was selected in order to represent the measured efficiency at neutron energies from 1 MeV to 4 MeV.

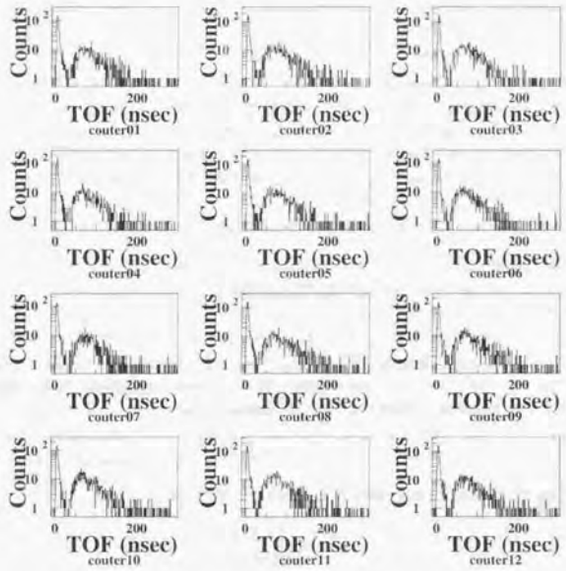

Figure A.1: TOF spectrum of the measurement with the fission source. The horizontal axis is the TOF (nsec) and the vertical axis is the event number. The TOF was derived by averaging the timing signals from both side of the neutron counter. The γ-flash peak is at 5 nsec.

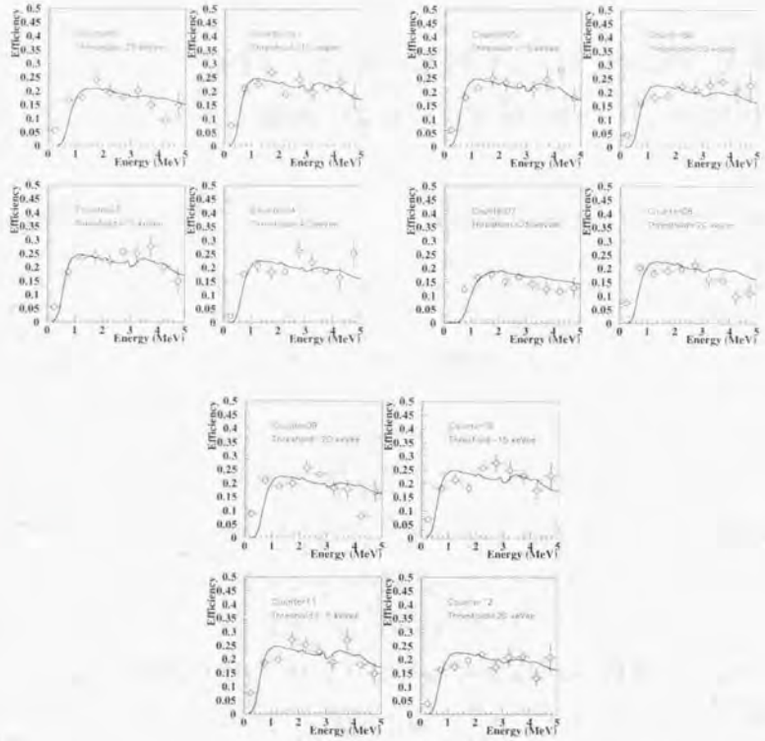

Figure A.2: Efficiency curves of the neutron counters. The horizontal axis is the neutron energy (MeV) and the vertical axis is the efficiency. The circles with error bars show the measured value and the solid curve shows the result of a simulation.

Appendix B

Formalisms relevant to the astrophysical calculation

B.1 Astrophysical S factor

The astrophysical S factor, $S(E)$, is defined as

$$S(E) = \sigma(E) E \exp(2\pi\eta) \ . \tag{B.1}$$

where η is the Sommerfeld constant, described as

$$\begin{aligned} \eta &= \frac{Z_i Z_j}{\hbar v} \\ &= \frac{1}{2\pi}\sqrt{\frac{E_G}{E}} \ . \end{aligned} \tag{B.2}$$

where E_G is the Gamov energy, described as

$$\begin{aligned} E_G &= 4\pi^2 \left(\frac{Z_i Z_j}{\hbar v}\right)^2 \left(\frac{1}{2} A v^2\right) \\ &= 0.9791 A Z_i^2 Z_j^2 \quad [\mathrm{MeV}] \ . \end{aligned} \tag{B.3}$$

Thus, the excitation function of the cross section, $\sigma(E)$, is written with the astrophysical S factor as

$$\sigma(E) = \frac{exp(-\sqrt{\frac{E_G}{E}})}{E} S(E) \ . \tag{B.4}$$

B.2 Reaction rate

It is relevant to divide equation 6.2 into four energy regions where the different reaction mechanisms are dominant. The features of the individual reaction mechanisms are illustrated in figure B.1.

According to Appendix A in reference [51], the reaction between charged particles is described as

$$< \sigma v > = < \sigma v >_{nr} + \sum < \sigma v >_r + < \sigma v >_{ur} + < \sigma v >_{sc} \ , \tag{B.5}$$

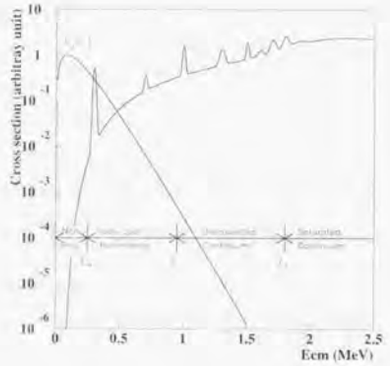

Figure B.1: Illustration of the typical types of reactions between charged particles. See the text for details. The horizontal axis is the center-of-mass energy in MeV and the vertical axis is the cross section in arbitrary units. The Maxwell-Boltzmann distribution of $T_9 = 1$ is also plotted in arbitrary units as a function of the center-of-mass energy (MeV).

The first term, $< \sigma v >_{nr}$, represents the components of the non-resonant reactions, which occurs at the very low-energy region between 0 MeV and near to the first resonance energy, E_N. This term is usually unimportant for a charged-particle reaction, because the first resonance is dominant.

The second term, $\sum < \sigma v >_r$, represents the component of the individual-resonant reactions which occur at the energy region between E_N and E_I, where the total width, Γ, of an individual resonance is much less than the effective width, δE_0 (see equation B.15~B.17). This term is described as

$$\sum < \sigma v >_r = \sum_{resonance\,r} C_r T_9^{-3/2} \exp(-E_r/kT_9) \ , \tag{B.6}$$

where E_r is the center-of-mass energy for a resonance r and C_r is described as

$$C_r = \frac{1.54 \times 10^{11}(1+\delta_{ij})(2J_r+1)}{A^{3/2}(2J_i+1)(2J_j+1)} \left(\frac{\Gamma_1\Gamma_2}{\Gamma}\right)_r \ [\mathrm{cm}^3/\mathrm{sec}/\mathrm{gr}] \ . \tag{B.7}$$

The third term, $< \sigma v >_{us}$, represents the component of the unsaturated continuum where many resonance state are located within δE_0, and the individual property of the resonance is indistinguishable. Between E_I and the Coulomb barrier, E_C, this term is described as

$$< \sigma v >_{uc} \sim F_u T_9^{-2/3} exp[-\tau_c T_9^{-1/3} - (T_9/T_u^*)^2] \tag{B.8}$$

$$\tau_c = 4.2487 A^{1/3} (Z_i Z_j)^{2/3} \tag{B.9}$$

$$T_u^* = 28.2 A^{-1/2} (Z_i Z_j)^{-1} E_C^{3/2} \ , \tag{B.10}$$

where τ_c and T_u^* are cutoff parameters, and F_u is a constant. In the case of the (α,n) and (p,n) reaction, the factor of $(T_9/T_u^*)^2$ is usually unnecessary.

The fourth term at $E > E_C$, $< \sigma v >_{sc}$, represents the components of the saturated continuum. If the ejectile is a photon, or the ejectile penetration factor does not greatly vary over the interested energy region, this term is described as

$$< \sigma v >_{sc} \sim H \exp(-E_C/kT_9) , \tag{B.11}$$

where H is a constant.

The contribution to the total reaction rate of each term depends on the effective energy and energy width, which are determined by the temperature. The effective energy, E_0, and energy width, δE_0, are represented by the center energy and the width of the Gamov peak, which is due to the penetration factor and the Maxwell-Boltzmann distribution function at the temperature.

When the center-of-mass energy, E, is below the Coulomb barrier, E_C, E_0 and δE_0 are described as follows:

$$\begin{aligned} E_0 &= 0.122 A^{1/3} (Z_i Z_j T_9)^{2/3} \ \text{[MeV]} && \text{(B.12)} \\ &\sim 0.12 (Z_i T_9)^{2/3} \ \text{[MeV]} \ (j = \text{proton}) && \text{(B.13)} \\ &\sim 0.30 (Z_i T_9)^{2/3} \ \text{[MeV]} \ (j = \alpha\text{-particle}) , && \text{(B.14)} \end{aligned}$$

$$\begin{aligned} \delta E_0 &= 0.237 A^{1/6} (Z_i Z_j)^{1/3} T_9^{5/6} \ \text{[MeV]} && \text{(B.15)} \\ &\sim 0.24 Z_i^{1/3} T_9^{5/6} \ \text{[MeV]} \ (j = \text{proton}) && \text{(B.16)} \\ &\sim 0.37 Z_i^{1/3} T_9^{5/6} \ \text{[MeV]} \ (j = \alpha\text{-particle}) . && \text{(B.17)} \end{aligned}$$

Here the Coulomb barrier

$$E_C = 1.44 Z_i Z_j / R \ \text{[MeV]} , \tag{B.18}$$

where

$$\begin{aligned} R &= 1.07 A_i^{1/3} + 2.17 \ \text{[fermi]} \ (j = \text{proton}), && \text{(B.19)} \\ R &= 1.07 A_i^{1/3} + 3.01 \ \text{[fermi]} \ (j = \alpha\text{-particle}), && \text{(B.20)} \end{aligned}$$

is usually used.

Appendix C

Another example of a measurement using MSTPC and future improvements

C.1 ^{6}He+Ar fusion reaction

A test experiment to measure the ^{6}He+^{nat}Ar fusion reaction was also carried out with the RIPS. A low-energy ^{6}He beam was produced by the same procedure as ^{8}Li, irradiating a 70 MeV/nucleon ^{11}B beam on a 1663mg/cm^2 thick ^{9}Be target at an intensity of 26pnA, and injected in the MSTPC at an energy of $10 \sim 20$ MeV with an intensity of 4 kcps. The MSTPC was filled with gases of ^{nat}Ar admixed with 2% of methane at 100 torr. The anode voltage was set to +600 V and the field voltage was set to -150 V, where the drift velocity was about 2 cm/μsec. In this case, the event trigger consisted of the beam counter and the dE/dx-discriminator signals.

Though quasi-elastic scattering could be mixed to the fusion trigger, if the scattering angle was large, the background events might be selected by the dE/dx and trajectory pattern at the stage of an off-line analysis. The typical fusion-like event is shown in figure C.1. dE/dx changes suddenly at the reaction point and stops soon a few pads ahead. Figure C.2 shows a typical quasi-elastic scattering event at a large angle. Although dE/dx changes suddenly at the reaction point due to the recoiled target and the trajectory changes, the ejectile runs longer than the fusion-like event.

Due to the narrow dynamic range of the F-ADC, the sampled dE/dx of a fusion-like event is saturated. In order to classify whether the event is complete fusion or incomplete fusion, the summed energy of the cathode pads from the reaction point to the end point of a range should be measured. Thus, a 12-bit PH-ADC module was also employed in parallel to a F-ADC module.

This method has been found to be powerful for measuring a fusion-like event in the subbarrier energy region.

C.2 Further improvement

We have some ideas for improving the MSTPC.

In order to improve the energy resolution, the anode-wire signals of the MSTPC should be read out by adding readout devices.

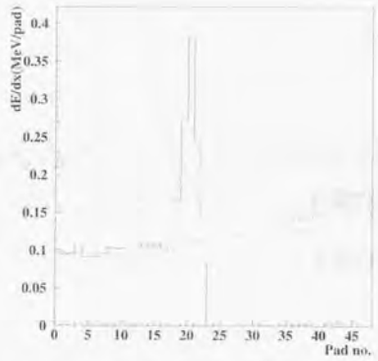

Figure C.1: Typical event of a fusion-like reaction. dE/dx changes at the reaction point and the ejectile particle stops soon. The dE/dx signal was saturated at the reaction point. The dashed line shows the Bragg curve of ^{6}He.

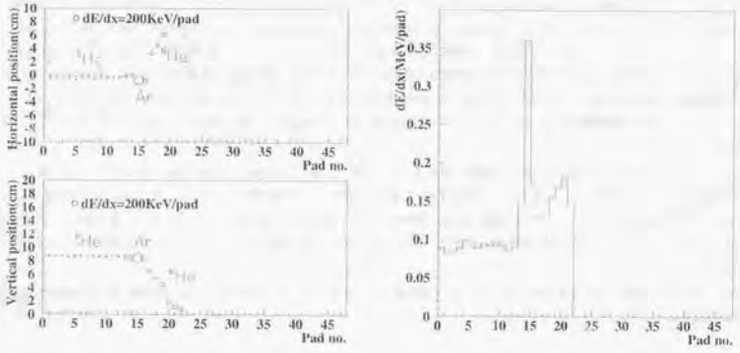

Figure C.2: Typical event of the quasi-elastic scattering. The left side shows the trajectory pattern and the right side shows the dE/dx pattern. dE/dx changes at the reaction point, but the ejectile does not stop soon.

Due to the space-charge limit of the gas counter, an experiment with a high-intensity beam, e.g. over 10 kcps, is difficult to perform. For an experiment with a higher beam intensity, a gating grid [52] will be installed in the near future.

In addition, we have some ideas for a measurement method. A trigger counter, like a MWPC or a plastic scintillator, can be installed in the vacuum chamber at the outer sides of the field cage. If this setup were available, the I(α,p)J and I(p,α)J-type reactions, which are also interesting for astrophysical nuclear reactions, could be measured by detecting the ejectile p or α particle by a side trigger counter.

The reaction type which can be measured by the MSTPC is mainly a reaction with a sudden change in dE/dx, especially a fusion-like reaction. In the case of a reaction with a small dE/dx change, like a transfer reaction, a measurement may be carried out, if an appropriate trigger counter is available.

Some of the suggestions and ideas will be realized in the next MSTPC.

References

[1] G. Börner, *The Early Universe. Third Edition*, (Springer-Verlag, 1993)

[2] E. W. Kolb, and M. S. Turner, *The Early Universe*, (Addison-Wesley, 1993)

[3] N. A. Bahcall, L. M. Lubin, and V. Dorman, *Astrophys. J. Lett.* **447**, 81 (1995)

[4] L. P. David, C. Jones, and W. Forman, *Astrophys. J.* **445**, 578 (1995)

[5] C. Alcock, G. M. Fuller, and G. J. Mathews, *Astrophys. J.* **320**, 439 (1987).

[6] J. H. Applegate, and C. J. Hogan, *Phys. Rev.* D **31**, 3037 (1985).

[7] J. H. Applegate, C. J. Hogan, and R. J. Scherrer, *Phys. Rev.* D **35**, 1151 (1987).

[8] T. Kajino, and R. N. Boyd, *Astrophys. J.* **359**, 267 (1990).

[9] L. H. Kawano, W. A. Fowler, R. W. Kavanagh, and R. A. Malaney, *Astrophys. J.* **1**, 372 (1991).

[10] R. A. Malaney, and W. A. Fowler, *Astrophys. J.* **333**, 14 (1988).

[11] G. J. Mathews, T. Kajino, and M. Orito, *Astrophys. J.* **456**, 98 (1996).

[12] T. Paradellis, S. Kossionides, G. Doukellis, X. Aslanoglou, P. Assimakopoulos, A. Pakou, C. Rolfs, and K. Langanke, *Z. Phys.* A **337**, 211 (1990)

[13] K. Kimura, Y. Akiba, Y. Miake, and S. Nagamiya, *Nucl. Instrum. Methods* **297**, 190 (1990)

[14] R. N. Boyd, I. Tanihata, N. Inabe, T. Kubo, T. Nakagawa, T. Suzuki, M. Yonokura, X. X. Bai, K. Kimura, S. Kubono, S. Shimoura, H. S. Xu, and D. Hirata, *Phys. Rev. Lett.* **68**, 1283 (1992)

[15] X. Gu, R. N. Boyd, M. M. Farrell, J. D. Kalen, C. A. Mitchell, J. J. Kolata, M. Belbot, K. Lamkin, K. Ashktorab, F. D. Becchetti, J. Brown, D. Robers, K. Kimura, I. Tanihata, K. Yoshida, and M. S. Islam, *Phys. Lett.* B **343**, 31 (1995)

[16] S. Kubono, R. Boyd, N. Ikeda, M. H. Tanaka, T. Nomura, Y. Fuchi, H. Kawashima, M. Ohura, H. Orihara, S. Yun, H. Toyokawa, M. Yosoi, H. Ohnuma, I. Tanihata, and T. Kajino, *Z. Phys.* A **338**, 459 (1991).

[17] S. Kubono, N. Ikeda, M. H. Tanaka, T. Nomura, I. Katayama, Y. Fuchi, H. Kawashima, M. Ohura, H. Orihara, C. C. Yun, Y. Tajima, M. Yosoi, H. Ohnuma, H. Toyokawa, H. Miyatake, T. Shimoda, R. N. Boyd, T. Kubo, I. Tanihata, and T. Kajino, *Z. Phys.* A **341**, 121 (1991).

[18] Z. Q. Mao, R. B. Vogelaar, and A. E. Champagne, *Nucl. Phys.* A **567**, 111 (1991).

[19] Z. Q. Mao, R. B. Vogelaar, A. E. Champagne, J. C. Blackmon, R. K. Das, K. I. Hahn, and J. Yuan, *Nucl. Phys.* A **567**, 125 (1994).

[20] Y. Mizoi, T. Fukuda, Y. Matsuyama, T. Miyachi, J. Nakano, N. Fukuda, M. Hirai, H. Kobinata, Y. X. Watanabe, H. Sakurai, Y. Watanabe, and A. Yoshida,*Nucl. Instrum. Methods* A **431**, 112 (1999)

[21] A. Yoshida, N. Aoi, T. Fukuda, M. Hirai, M. Ishihara, H. Kobinata, Y. Mizoi, L. Mueller, Y. Nagashima, J. Nakano, T. Nomura, Y. H. Pu, F. Scarlassala, C. Signorini, and Y. Watanabe, *Nucl. Phys.* A **588**, 109c (1995)

[22] A. Yoshida, C. Signorini, T. Fukuda, Y. Watanabe, N. Aoi, M. Hirai, M. Ishihara, H. Kobinata, Y. Mizoi, L. Mueller, Y. Nagashima, J. Nakano, T. Nomura, Y. H. Pu, and F. Scarlassara, *Phys. Lett.* B **389**, 457 (1996)

[23] W. B. Christie, J. L. Romero, F. P. Brady, C. E. Tull, C. M. Castaneda, E. F. Baraseh, M. L. Crawford, I. Flores, D. E. Greiner, P. J. Lindstrom, H. Sann, and J. C. Young, *Nucl. Instrum. Methods* A **255**, 466 (1987)

[24] C. N. Davids, *Nucl. Phys.* A **110**, 619 (1968)

[25] K. W. Geiger, and L. Van Der Zwan, *Nucl. Instrum. Methods* **131**, 315 (1975)

[26] A. W. Obst, T. B. Grandy, and J. L. Weil, *Phys. Rev.* C **5**, 738 (1972)

[27] P. R. Wrean, C. R. Brune, and R. W. Kavanagh, *Phys. Rev.* C **49**, 1205 (1994)

[28] L. Van Der Zwan, and K. W. Geiger, *Nucl. Phys.* A **152**, 481 (1970)

[29] T. Kubo, M. Ishihara, N. Inabe, H. Kumagai, I. Tanihata, K. Yoshida, T. Nakamura, H. Okuno, S. Shimoura, and K. Asahi, *Nucl. Instrum. Methods* B **70**, 309 (1992)

[30] Y. Yano, *Proc. 12th Int. Conf. on Cyclotrons and their Applications*, Berlin, eds. B. Martin and K. Ziegler (World Scientific, 1989) P.13

[31] J. A. Winger, B. M. Sherrill, and D. J. Morrissey, *Nucl. Instrum. Methods* B **70**, 380 (1992)

[32] J. P. Dufour, R. Del Moral, H. Emmermann, F. Hubert, D. Jean, C. Poinot, M. S. Pravikoff, A. Fleury, H. Delagrange, and K. -H. Schmidt, *Nucl. Instrum. Methods* A **248**, 267 (1986)

[33] R. A. Cecil, B. D. Anderson, and R. Madey, *Nucl. Instrum. Methods* **161**, 439 (1979)

[34] M. Sasaki, *Master thesis*, Osaka University, 1995

[35] N. Aoi, K. Yoneda, H. Miyatake, H. Ogawa, Y. Yamamoto, E. Ideguchi, T. Kishida, T. Nakamura, M. Notani, H. Sakurai, T. Teranishi, H. Wu, S. S. Yamamoto, Y. Watanabe, A. Yoshida, and M. Ishihara, *Nucl. Phys.* A **616**, 181c (1997).

[36] H. Miyatake, Y. Yamamoto, T. Shimoda, S. Tanimoto, S. Mitsuoka, H. Ueno, H. Izumi, H. Ogawa, K. Asahi, N. Aoi, Y. Mizoi, M. Notani, K. Yoneda, M. Ishihara, E. Ideguchi, A. Ozawa, T. Kubo, and T. Kishida, *RIKEN Accel. Prog. Rep.* **30**, 59 (1997).

[37] G. Hardie, B. W. Filippone, A. J. Elwyn, M. Wiescher, and R. E. Segel, *Phys. Rev.* C **29**, 1199 (1984)

[38] Y. Mizoi, J. Nakano, Y. Matsuyama, T. Fukuda, M. Hirai, H. Kobinata, Y. Watanabe, H. Sakurai, Y. Watanabe, A. Yoshida, T. Kishida, and K. Kimura, *INS Ann. Rep.* **1994**, 49 (1995)

[39] M. Hirai, *Master thesis*, University of Tokyo, 1995

[40] R. Allemand, and G. Thomas, *Nucl. Instrum. Methods* **137**, 141 (1976)

[41] T. K. Taniguchi et al., *KEK-85-10* (85.REC.JAN.86) 40p.

[42] H. Kobinata, *Master thesis*, University of Tokyo, 1996

[43] Y. Yasu et al., *KEK-PREPRINT-94-137*, Nov 1994, 10p.

[44] Y. Yasu et al., *KEK-PREPRINT-95-84*, Jul 1995, 4p.

[45] J. F. Ziegler, *Handbook of Stopping Cross-Sections for Energetic Ions in All Elements* (Pergamon, New York, 1980), Vol.5.

[46] T. Rauscher, K. Grün, H. Krauss, and H. Oberhummer, *Phys. Rev.* C **45**, 1996 (1992)

[47] P. Descouvemont, *Nucl. Phys.* A **596**, 285 (1996)

[48] Y. Yamamoto, *private communication*, CNS, university of Tokyo

[49] C. Wagemans, *The Nuclear Fission Process*, C R C Press, Incorporated, January 1991

[50] J. van Aarle, W. Westmeier, R. A. Esterlund, and P. Patzelt, *Nucl. Phys.* A **578**, 77 (1994)

[51] R. V. Wagoner, *Astrophys. J. Suppl.* **18**, 247 (1969)

[52] P. Némethy, P. J. Oddone, N. Toge, and A. Ishibashi, *Nucl. Instrum. Methods* **212**, 273 (1983)